Revision 1

Word Count: 9721

Oriented triphylite rods in apatite from an LCT pegmatite in the Stankuvatske Li-ore deposit, Ukraine: implications for Li mobility

SERGII KURYLO[1], IGOR BROSKA[2], AND GIERÉ RETO[3]

[1]Earth Science Institute, Slovak Academy of Sciences, Ďumbierska 1, Banská Bystrica, 974 11, Slovakia;

[2]Earth Science Institute, Slovak Academy of Sciences, Dúbravská cesta 9, 840 05 Bratislava, Slovakia

[3]Department of Earth and Environmental Science, University of Pennsylvania, Philadelphia, U.S.A.

ABSTRACT

The present paper reports the first finding of oriented triphylite ($LiFe^{2+}PO_4$) rods in fluorapatite. This observation was made in the contact zone between a metamorphosed rare-element pegmatite and its amphibolite wall rock at the Stankuvatske Li-ore deposit in the Ukrainian Shield. This contact zone consists of an exocontact, in which hornblende was altered to biotite, and an endocontact, which comprises four parallel mineral zones (aplitic, apatite, triphylite, and transitional).

The needle-shaped triphylite inclusions were observed in greenish-blue apatite within the apatite zone. They are oriented parallel to structural nanochannels along the *c*-axis in apatite, and were formed due to infiltration of Li-rich, pegmatite-derived fluids into the apatite zone. Small amounts of pyrite, U-Th-rich and Fe-rich phases, as well as small mono-phase

fluid inclusions of CO_2, CO, and N_2 are associated with the oriented triphylite inclusions and record the character of fluid.

The exo- and endocontacts were formed as a result of interaction between metasomatic fluids derived from the pegmatite (enriched in K, Na, Li, Rb, F, P, and Mn) with the host amphibolite. At the contact, the amphibolite was altered into the biotite zone during the first metasomatic stage; alteration of hornblende and plagioclase released Ca, Fe, and Mg towards the pegmatite, where these elements reacted with P, Li and Mn to produce the apatite and triphylite zones during the second metasomatic stage. Acting like a geochemical barrier, the apatite zone in the endocontact, inhibited the further escape of Li from the pegmatite, which now is a Li-ore deposit. The metasomatic processes observed in the Stankuvatske Li-ore deposit represent an example of apatite and triphylite formation at the contact between a pegmatite and a metabasite, which has metallogenetic implications.

Keywords: contact zone, apatite, triphylite, triphylite rods, fluid interaction, Ukrainian Shield.

INTRODUCTION

Apatite can incorporate high contents of many elements into its structure, especially in alkaline igneous rocks and carbonatites, and at (ultra)high-pressure (UHP) conditions. Initially high contents of trace elements in apatite are prone to be released again by fluid interaction or decompression from UHP conditions, resulting in the formation of various mineral phases in apatite, such as monazite inclusions, e.g. in form of oriented rods (Pan et al. 1993a; Zhang and Liou 1999; Zhu and Massonne 2005; Harlov et al. 2005; Ziemann et al. 2005; Sun et al. 2007; Krenn et al. 2008) (Supplementary table S1). The origin of monazite and xenotime inclusions in apatite has been inferred to be due to infiltration of fluids and interpreted as a consequence of dissolution-reprecipitation processes (Harlov et al. 2002,

2005). Generally, fluid activity can easily affect the apatite-type structure, especially by flow through structural nanochannels along the *c*-axis of apatite (Kato et al. 2018). In this context, oriented pyrrhotite inclusions in apatite that underwent decompression from UHP conditions were also explained by the high activity of volatile sulfur and interactions with Fe along apatite nanochannels (Broska et al. 2014).

The aim of the current article is to describe for the first time the occurrence of oriented triphylite rods in green apatite, as observed at the Stankuvatske Li deposit in Ukraine. Here, apatite and triphylite are present in a rare-element pegmatite, and our observations point to an important role of apatite as a geochemical barrier for light elements (Li, F, P) in metallogenetic processes.

GEOLOGICAL SETTING

The petalite- and spodumene-pegmatite dikes are located in the north-western part of the Lypniazhka Dome Structure in the western Inhul Domain of the Ukrainian Shield (Fig. 1). In planar view, the NW-trending Lypniazhka Dome structure displays a crystalline core consisting of the Proterozoic Kirovohrad granite complex, dated at ~2032–2026 Ma (Stepanyuk et al. 2018). The host rocks of these granitoids comprise Paleoproterozoic to Neoarchean amphibolites, ultrabasites, and gneisses (2450 to 2650 Ma) (Yesypchuk et al. 2004). Gneisses have been metamorphosed in upper amphibolite facies at ~620–680°C and 500-600 MPa (Sherbakov 2005), and amphibolites at approximately 650−710°C and 270−350 MPa (Kurylo et al., unpublished data).

The Stankuvatske Li deposit (SLD) is the largest and the best-studied deposit in the area, representing granitic pegmatite dikes, which were intruded into amphibolite and ultrabasic rocks parallel to the host rocks foliation (Ivanov et al. 2011) and subsequently overprinted by varying degrees of hydrothermal-metasomatic and tectonic activity yielding

metapegmatites. The time relationship between pegmatite crystallization and tectonic overprint, however, is unknown due the absence of isotope dating of the SLD pegmatites. The thickness of the Li-bearing pegmatite dikes ranges from 1 to 33 m. The SLD pegmatites are coeval with the Kirovohrad granite complex (Shcherbak et al. 2008; Stepanyuk et al. 2018, 2021). According to the classification of Černý and Ercit (2005), the studied pegmatite dikes show affinity to the rare-element class, specifically to the petalite or spodumene subtype of the LCT (Li-Cs-Ta) family. General mineralogical features of the Li-ore deposit were reported by Nechaev et al. (1991), Eremenko et al. (1996), Vozniak (2000, 2001), Ivanov et al. (2011), Hrinchenko et al. (2016), and recently by Kurylo et al. (2022). The contacts between the Li-rich metapegmatite dikes and the hosts rock amphibolite and ultrabasite are sharp and accompanied by metasomatic alteration, which led to the formation of biotite exocontact zones. The thickness of these biotite exocontact zones ranges from 0.5 to 1.5 cm, and they are characterized by an enrichment in Rb, Cs, Li, P, Be, Zn, Sn, Nb and Ta (Ivanov et al. 2000, 2011). Accessory apatite, holmquistite, taaffeite, chrysoberyl and phenakite have been described in this exocontact zone as well (Ivanov et al. 2000, 2011).

The metapegmatite dikes, referred to below simply as pegmatites, still contain remnants of a primary, pre-metamorphic magmatic assemblage, which is characterized by albite (more abundant than K-feldspar), quartz, and the Li-phases petalite and spodumene; rare triphylite and montebrasite; and accessory muscovite, fluorapatite, columbite, cassiterite, Ta-rich rutile, nigerite, gahnite, pyrite, sphalerite, and zircon. Hydrothermal–metasomatic alteration and subsequent metamorphic overprinting caused large-scale re-precipitation of Li phases, including formation of large quantities of green apatite. The general characteristics of the pegmatites were reported in detail by Syomka et al. (2022) and Kurylo et al. (2022).

SAMPLING AND RESEARCH METHODS

Metapegmatite drill core material (No 61-89, 34-91; locality 1 in Fig. 1b) from the Stankuvatske Li deposit provided the principal research material. The polished thin section from the crucial sample (61-89/240.5 m) for the present study was prepared for microprobe investigation. This specimen contains apatite, as detailed below, and comprises a range of rock types from the contact between the host amphibolite and the Li-bearing pegmatite dike. Other samples used for this study represent hand-picked apatite concentrates mounted in epoxy resin discs from drill core material of the Lypniazhka Li-ore mineralization (No 34-92, 77-90; locality 3 in Fig. 1b), which hosts similar apatite containing triphylite rods.

Sample locations are shown in Table 1. The rock-forming assemblages and the apatites were first investigated in polished thin sections under a polarized-light microscope. In addition, physical properties (color and inclusions) were studied on hand-picked apatite concentrates under a binocular microscope.

The mineral compositions were determined using a JEOL JXA 8530F field-emission electron microprobe (EMP) in wavelength-dispersive mode (WDS) at the Earth Science Institute of the Slovak Academy of Sciences in Banská Bystrica. The following analytical conditions were applied: probe current 20 nA; acceleration voltage 15 kV; beam diameter 3–10 μm; counting time 10–40 s on the peak, and 5–20 s on the background, depending on element concentrations. X-ray lines and standards used are shown in Table 2. The raw counts were converted to oxide wt% using a ZAF matrix correction. Based on the counting statistics, the measurement error, expressed as 3σ, is approximately < 0.6 rel. % at the >20 wt%, 3–6 rel.% at the 3–1 wt%, and < 20 rel. % at the 0.3 wt%.

The concentrations of F and Cl in apatite were determined according to the procedure described in Stormer et al. (1993). Halogen measurements were made at 15kV and 5nA, and with a 15 μm beam diameter spot in large crystals and between 5 and 10 μm in smaller

crystals. X-ray intensities were measured in accumulation mode with 5 measurements and a total counting time of 100 sec on the peak and 50 sec on the background on both sides. Apatite sections perpendicular to the *c*-axis were selected for analysis to minimize diffusion of F and Cl during electron irradiation. The measurement error for F is estimated at 3.2 rel.% at the 3 wt% level, that for Cl at 1.0 rel.% at the 2.5 wt% level, and 3.0 rel.% at the 0.5 wt% level.

EMP elemental X-ray maps of F, Fe, and Mn were made for one selected fluorapatite grain, at the accelerating voltage of 15kV and with a beam current of 150 nA; each pixel in the element maps represents 80 milliseconds of counting time.

Raman spectroscopic analyses were performed at the Geological Institute Academy of Science in Banská Bystrica using a Czerny-Turner monochromator with a 600 gr/mm grating, and a LabRam HR800 (Horiba Jobin-Yvon) spectrometer. The spectrometer is equipped with a Peltier-cooled CCD Synapse detector connected to an Olympus BX41 microscope. Raman spectra were excited by He-Ne (633 nm) and Nd-YAG (532 nm) lasers. A silicon wafer was used for calibration.

Cold-CL images were obtained using a CATHODYNE optical cathodoluminescence system (NewTec Scientific, France) at the Geological Institute of the Bulgarian Academy of Sciences, Sofia. Voltage was 6kV, current 60-80 μA, and pressure 70-80 mTorr.

Trace element analyses of the large apatite crystals and triphylite from the apatite and triphylite mineral zones (see below) were carried out using a New Wave Research (NWR) Excimer 193 nm laser-ablation system attached to a Perkin-Elmer ELAN DRC-e inductively coupled plasma mass spectrometer (LA–ICP–MS) at the Geological Institute, Bulgarian Academy of Science, Sofia. Spatial resolution was 35 μm and frequency 4-6 Hz. The measurement procedure involved calibration against an external standard (NIST610, Pearce et al. 1997) at the beginning, in the middle, and at the end of each analytical block. A secondary

149 standard (NIST 612) was measured for cross-checking the results. The LA-ICP-MS analyses
150 of the examined minerals were recalculated using the EMP-determined contents of CaO for
151 apatite and FeO for triphylite as internal standards. This technique allows for a suitable
152 correction of instrumental drift along with minimization of elemental fractionation effects.
153 Raw data were processed using SILLS software (Guillong et al. 2008).
154

155 ## MINERAL ZONES FORMED AT THE AMPHIBOLITE –PEGMATITE CONTACT

156 The pegmatite containing the investigated apatite with the triphylite rods is up to 4.0 m
157 thick, and is in contact with a dark-grey, fine-grained (0.3–0.8 mm) amphibolite host rock.
158 The amphibolite (sample 61-89/235 m) consists of magnesio- to ferrohornblende (Mg/(Mg +
159 Fe^{2+}) = 0.47–0.54; average Mg# [Mg/(Mg + Fe_{total})] = 0.39; MgO up to 8.2 wt%; MnO <0.4
160 wt%), plagioclase (An_{38-44}), ilmenite, and minor quartz, pyrite, chalcopyrite, arsenopyrite, and
161 löllingite; zircon and apatite are the most typical accessory phases.

162 At the contact between the amphibolite and the pegmatite, two alteration zones – an
163 exocontact and an endocontact – can be observed (Fig. 2). The exocontact formed in the host
164 amphibolite and is characterized by alteration of hornblende to biotite, whereas the
165 endocontact is located within the pegmatite and consists of a set of parallel mineral layers
166 formed by post-magmatic fluid activity, which overprinted the former mineral assemblage.

167 The *exocontact* biotite zone (BT) is the result of metasomatic alteration of host
168 amphibolite by the intruded pegmatite. It is 2 cm thick, dark-grey, and fine-grained (0.1 – 0.3
169 mm), and consists of light-brown biotite (Mg# 0.58–0.60; MgO up to 12.9 wt%;) after
170 hornblende (Fig. 2), subhedral plagioclase (An_{32}; P_2O_5 <0.1 wt%), quartz,
171 magnesioholmquistite, and fluorapatite. Biotite and plagioclase display a foliation parallel to
172 the pegmatite contact. Magnesioholmquistite forms small (<12 μm), homogenous grains with
173 (Fe / (Mg + Fe)) between 0.41 and 0.44, and an MnO content <0.31 wt%.

The *endocontact* is mineralogically more complex than the exocontact (Fig. 2), but its thickness of ca 2.5 cm is similar. It comprises four thin, mineralogically distinct zones, arranged in the following sequence from the edge of the host amphibolite to the pegmatite: (1) aplitic, (2) fluorapatite, (3) triphylite, and (4) transition to pegmatite.

The aplitic zone (APL) is ca 5 mm wide and can be subdivided into two subzones APL1 and APL2. Subzone APL1 is closest to the host amphibolite, and is equigranular and fine-grained (0.5–2.0 mm), consisting of euhedral to subhedral plagioclase (An_{27-10}; P_2O_5 up to 0.5 wt%), anhedral quartz, and fluorapatite. Albite and quartz crystals exhibit an elongation parallel to the contact zone. Further away from the host amphibolite is aplitic subzone APL2 (Fig. 2), which does not contain quartz, but consists of mostly albite ($An_{<10}$; P_2O_5 content up to 0.8 wt%) and abundant prismatic apatite. The APL2 subzone contains minor amounts of niobian rutile, rarely ilmenite, and locally fibrous spodumene. Aplitic relic fragments of the APL2 subzone, which are up to 2.2 mm in size, are enclosed in the apatite and triphylite zones, and consist of some albite (An_{7-8}; P_2O_5 content up to 1.6 wt%), secondary fibrous spodumene, minor K-feldspar, magnesioholmquistite, and apatite. The relic APL2 fragments in the apatite zone contain an assemblage of ferroholmquistite, quartz, K-feldspar, albite, chlorite, schorl, pyrite, and graphite. Ferroholmquistite forms (1) mineral aggregates up to 500 μm in length consisting of tiny ferroholmquistite needles (<5 μm wide each), and (2) individual crystals up to 180 μm within the apatite zone. In contrast to magnesioholmquistite occurring in the BT zone, ferroholmquistite has an Fe / (Fe + Mg) value between 0.82 and 0.85, and contains up to 0.73 wt% MnO.

The apatite zone (AP) has a width of 3.5–4.5 mm and consists mainly of apatite, with some primary rock-forming relics from the pegmatite (<5 vol. %). Fluorapatite is greenish-blue and prismatic, ranges in size from 1.0 to 2.5 mm, and contains tiny, needle-shaped inclusions of triphylite (as detailed below), which have also been detected in Raman spectra.

The apatite crystals are aligned parallel to the pegmatite/amphibolite contact. Within the AP zone, the accessory mineral assemblage tantalite–columbite, cassiterite, niobian rutile, ilmenite, and gahnite is present, mainly along the apatite–albite boundaries.

The triphylite zone (TR) has a width of 1.0–1.2 cm. It exhibits a light green color in the hand specimen and a pale greenish yellow color under the optical microscope, and consists of triphylite and relics of albite (Fig. 2, 3d,10a). Triphylite forms tabular crystals 0.5–2.5 mm in size. Locally triphylite contains tiny chrysoberyl inclusions and greenish tourmaline (identified only optically). In contrast to the AP zone, an oxide mineral assemblage is missing.

The transitional zone (TRN) is located between the AP zone and the main pegmatite body. It is fine- to medium-grained (0.3–1.5 mm), consists of anhedral, pale yellow triphylite (<100 μm) and euhedral to subhedral albite ($An_{6–8}$; P_2O_5 content up to 1.25 wt%), with subordinate K-feldspar. Accessory minerals present are apatite, zircon (as relics rimmed by cheralite or thorite), and ferroholmquistite, which is similar to the ferroholmquistite in the aplitic fragments (APL2). Fibrous spodumene is observed in grain interstices.

The adjacent pegmatite (PGM) rock (samples 61-89/240.5 m and 61-89/241.5 m) is fine-grained (0.1–0.6 mm) and consists of albite (compositionally similar to albite from the TRN), quartz, minor K-feldspar, petalite, and fibrous spodumene. Triphylite (up to 100 μm in size), apatite, niobian rutile, cassiterite, uraninite, and nigerite are the main accessory minerals.

Similar sequences of mineral zones at contacts between pegmatite and host metabasites were also found in the same drill cores but at different depths (drill core 61/89, 70.5 m and 125 m). The endocontact zone at a depth of 70.5 m is without continuous apatite and triphylite layers; rather apatite and triphylite form aggregates or lenses. Rare greenish-blue tourmaline and fine-grained euhedral chrysoberyl were also identified in the triphylite zone.

CHARACTERISTICS OF THE PHOSPHATE MINERALS

Apatite

Three types of apatite (A1, A2, A3) have been distinguished on the basis of their textural characteristics and chemical compositions. They occur in different parts of the pegmatite-amphibolite contact zone, with a summary of their petrographic and compositional features given in Table 3. Representative microprobe analyses of apatite from all investigated zones are given in the Tables 4, 5, and Supplementary Material Table S2A.

A1-type apatite. This apatite is abundant in the aplitic zones (APL1 and APL2, including aplitic relics), and occurs in lesser amounts in the adjacent amphibolite (AMP), as well as in the BT, TRN and PGM zones (Fig. 3). Compositionally, the A1-type apatite lies between hydroxyl- and hydroxyl-rich fluorapatite. The crystals are colorless, elongated and needle-shaped (10–200 μm), locally up to 2 mm long, and are usually included in plagioclase without preferred crystallographic orientation. Prismatic stubby apatite was observed in the rims of plagioclase and/or in between plagioclase crystals, where plagioclase is characterized by primary P enrichment (up to 1.6 wt% of P_2O_5) in the cores. The mole fraction of F (X_F = F/(F+OH+Cl)) decreases with increasing distance from the BT zone (~0.8) to the APL1, APL2, and AP zones (0.65–0.67), and to the adjacent pegmatite (0.21) (Fig. 4a). In the AMP, X_F in apatite is low (~ 0.5). The MnO content increases from the AMP to the BT and APL2 zones (from 0.06 to 1.32 wt%), and then gradually decreases toward the pegmatite (~0.5 wt%) (Fig. 4b).

A2-type apatite. Apatite of this type defines the AP zone, where it forms blue to greenish-blue, semi-euhedral stubby grains with a length of 1.0 to 2.5 mm (Fig. 5). The A2-type apatite is fluorapatite, with an X_F between 0.6 and 0.67 (Fig. 4a), and a very low X_{Cl} (< 0.02). Apatite from the AP zone has high MnO (up to 1.75 wt%) (Fig. 4b) and low FeO contents (<0.25 wt%), with an average Mn/Fe value of 8.8. The A2-type apatites in the

studied mineral concentrates display similar compositional characteristics, except for those in APM2 (pegmatite sample 34-91/113-114 m), which contains low amounts of MnO (Fig. 4b). X-ray element distribution maps and EMP cross-section analyses document internal chemical heterogeneity in A2-type crystals (Fig. 6). In its central part, the A2-type apatite shows higher Mn and Fe, but lower F contents compared to its rims (Fig. 6b, c). This zoning can be observed also in high-contrast BSE images, as indicated by the darker rims (Fig. 6a). The MnO content in the central parts may be as high as 1.74 wt%, whereas in the rim it is only 0.84 wt%. Similarly, FeO occurs in higher concentration in the apatite core (up to 0.21 wt%), but some parts show patchy inhomogeneities. It is of note that a higher concentration of triphylite needles is observed in the Mn-poor apatite domains (Fig. 6b, d; Supplementary Material Table S2B). Apatite commonly exhibits homogenous dark yellow luminescence. Locally, some apatite domains display a light-yellow color (Fig. 5d), which is correlated with higher MnO content in apatite and / or triphylite-poor domains.

LA-ICP-MS analyses (Table 5) of A2-type apatite from the AP zone are provided for the apatite grains that are well-documented by X-ray elemental maps and EMP cross-section analyses. The analysis spots where selected in both Mn-rich and Mn-poor apatite domains, where no inclusions of triphylite needles were visible. Apatite crystals display low contents of Na (87-140 ppm), Sr, and Al, and Si contents are close to the detection limit. Total REE content is low (from 215 to 306 ppm), the content of HREE (Gd to Lu plus Y) is higher than that of LREE (La to Eu), the LREE/HREE ratio is between 0.73 and 0.74. The U and Th contents range between 211 and 418 ppm and 108 and 33 ppm, respectively. It is noteworthy that the highest content of Th was detected in Mn-rich domains of apatite (Table 5, analyses 1 and 4), where it is two times higher than in the Mn-poor domains (Table 5, analyses 2, 3 and 5). Moreover, Mn-rich domains in apatite display slightly higher amounts of REE, U, Th, and

Sr compared to the Mn-poor domains. The Li content exhibits an opposite trend, with up to 43 ppm in Mn-rich and <8 ppm in the Mn-poor domains.

This A2-type apatite also contains tiny triphylite-needle inclusions oriented along its *c*-axis, as proven by characteristic Raman spectra (Fig. 7a, b; for description of triphylite rods please see Triphylite section). In addition to the oriented triphylite inclusions, apatite also contains inclusions of other minerals, albeit in much smaller amounts (pyrite, U-Th-rich and Fe-rich phases, cassiterite ilmenite, columbite). Some of these phases, including tiny (1-3 μm across) hematite crystals (identified by both EMP and Raman spectroscopy), may be intergrown with the triphylite needles (see below).

Almost all A2-type crystals also contain small mono-phase fluid inclusions, which occur in the form of stripes and spots in two dimensions. Raman spectroscopy revealed that these fluid inclusions have complex compositions: a typical spectrum displays two sharp bands at 1284 cm^{-1} and 1389 cm^{-1} (CO_2), as well as bands at 2140 cm^{-1} (CO) and 2329 cm^{-1} (N_2) (Fig. 7c). Water-containing inclusions were not detected.

A3-type apatite. This apatite is a late metasomatic phase, which either occurs as irregular veins (<10 μm) in triphylite from the TR zone or forms alteration parts in triphylite from the TRN and PGM zones. This apatite is clearly recognized by its yellow, brown-yellow luminescence (Fig. 8a, b). The A3-type apatite is typically associated with sulfides (pyrrhotite, less commonly pyrite and sphalerite) and rarely with carbonate ($Sd_{70-80}Rds_{14-17}Dol_{5-11}$). In contrast to the A1- and A2-type apatite, it is a Cl-rich hydroxylapatite, has a higher content of FeO (1.05 – 2.2 wt%) and an MnO content varying from 0.2 to 1.6 wt%, and contains detectable amounts of Na_2O (<0.58 wt%) and SrO (<0.53 wt%); the SO_3 content is up to 0.54 wt% (Table 4, analyses 10–12). The content of F is below the EMP detection limit, and X_{Cl} ranges between 0.34 and 0.45. However, analyses of A3-type apatites show a

297 relatively low P_2O_5 content (39 to 41 wt%) and thus, exhibit low T-site totals, pointing to the
298 presence of up to 1.68 wt% CO_2.

299 The Raman spectra obtained for the A1- and A2-type apatites display similar
300 characteristics in all mineral zones (Fig. 9). Representative Raman spectra display a vibration
301 band at 430 cm^{-1} and 442 cm^{-1} (ν_2), group bands at 582 cm^{-1}, 592 cm^{-1}, and 605 cm^{-1} (ν_4), and
302 a strong and sharp band at ~965 cm^{-1} (ν_1); in addition, they show a group of three strong bands
303 at 1041 cm^{-1}, 1052 cm^{-1}, and 1078–1080 cm^{-1} (Fig. 9b), and two weak bands at ~1114 cm^{-1}
304 and 1164 cm^{-1} (ν_3). The ν_1, ν_2, ν_3, and ν_4 vibration modes are due to the PO_4^{3-} symmetric and
305 stretching modes; however, the intensities of the modes ν_2, ν_3 and ν_4 are strongly dependent
306 on the crystal orientation. In contrast to the A1- and A2-type apatites, the late metasomatic
307 A3-type apatite, which replaced triphylite in the TRN zone, displays lower crystallinity with
308 less well-developed bands in the ν_2 and ν_4 (PO_4^{3-}) modes. In the region of the ν_3 bending
309 mode, two strong bands at 1048 and ~1078 cm^{-1}, and two weak bands at 1033 and 1041 cm^{-1}
310 have been observed (Fig. 9c). The vibration band at ~1078 cm^{-1} splits in two bands at 1070
311 and 1076 cm^{-1}, but these modes were not seen in the A1- and A2-type apatites.

312

313 **Triphylite**

314 The most abundant P phase is triphylite, which occurs in the PGM as well as in the TR
315 and TRN zones of the endocontact (Fig. 10); it is less abundant in the AP zone.
316 Representative EMP data of triphylite from all investigated zones are given in the Tables 5, 6
317 and Supplementary Material Tab. S3. In the PGM, triphylite has an average Fe/(Fe+Mn)
318 value of 0.83, and a MgO content between 1.3 and 2.1 wt%. In the TR zone, triphylite
319 exhibits weak Mg, Fe and Si oscillatory zoning; this zoning, however, was observed only
320 locally at the contact with the AP zone (Fig. 10b; the line of the EMP transect is given in the
321 Supplementary Material (Fig. S3).

In the TRN zone, triphylite occurs as homogenous grains, and is locally replaced by apatite and pyrrhotite (Fig. 10c, d). The compositions of triphylite from both the TR and the TRN zones are similar (Fig. 11): the Fe/(Fe+Mn) values range between 0.81 and 0.84, and the MgO contents reach (4.7 wt%). The LA-ICP-MS results (Table 5) show that triphylite from the TR and TRN zones contains extremely low contents of almost all analyzed trace elements, except for Zn, whose concentrations range from 864 to 1006 ppm; the Co content is also low (8.4 ppm on average). Triphylite from the TR zone displays slightly higher contents of Sc (~30 ppm) than triphylite from the TRN zone (~14 ppm). The concentration of Li_2O determined by LA-ICP-MS (10.09-11.7 wt%; 1.01 -1.133 apfu) is somewhat higher than that calculated from the empirical formula (9.68-9.77 wt% of Li_2O at 1.0 apfu).

A band of the symmetric stretching mode (ν_1) is located at ~ 950 cm^{-1}, which is the main and strongest band in the triphylite spectrum (Fig. 12). Two asymmetric stretching modes of the PO_4^{3-} anion (ν_3) are seen at ~1003 and ~1068 cm^{-1}. Three sharp bands were observed at ~576, 591 and ~ 628 cm^{-1}, which are due to the asymmetric vibration (ν_4) out of plane bending modes of the PO_4^{3-} units (Frost et al. 2013). A weak band at 403 and ~ 443 cm^{-1} can be assigned to the ν_2 PO_4^{3-} bending modes. A weak band at 325 cm^{-1} displays MnO stretching vibrations. The intensity of the vibration modes at 443 cm^{-1}, at 628 cm^{-1}, and at 1081 cm^{-1} are related to crystal orientation. The group of bands at 242, 252 and perhaps 291 cm^{-1} are attributed to external vibrations or vibrations of the lattice (Frost et al. 2013).

In the AP zone, triphylite occurs interstitially between apatite crystals and as needle-shaped rods within A2-type apatite. The interstitial triphylite is < 50 μm across, commonly associated with late pyrrhotite, and partially replaced by Cl-rich hydroxyl apatite (Fig. 13 a–c). This triphylite contains 2.84 – 3.13 wt% MgO and has an average Fe/(Fe+Mn) value of 0.72 (Table 6, analyses 4–8). The triphylite rods that are included in A2-type apatite from the AP zone vary in length between 20 and 800 μm and have widths between 1 and 5 μm.

These triphylite rods are commonly associated with U-Th-rich and Fe-rich phases, ilmenite, and cassiterite, and very rarely with columbite and galena (Fig. 13). Triphylite was confirmed by EMP as well as by Raman spectroscopy, where the typical vibrational bands at 626, 951, 1001, 1070 cm^{-1} were recorded (Fig. 7b). These inclusions contain low amounts of MgO (2.4–3.17 wt%, locally up to 3.98 wt%), are rich in MnO (10.04-12.6 wt%), and exhibit a Fe/(Fe+Mn) value of 0.70 (Fig. 11; Table 6, analyses 9–12, and Table S3), which is much lower than in the triphylite occurring in the TR zone (Table 5, analyses 1–3).

DISCUSSION

Textural observations at the pegmatite/amphibolite contact

The BT zone in the exocontact was formed as a result of the transformation of the host amphibolite by the pegmatite-derived K(Rb)- and F- rich fluids. During of this transformation, Ca, Fe and Mg were released from the host amphibolite and transported to the adjacent pegmatite. The A1-type apatite, with the highest X_F, is associated with F- and Rb-rich biotite and was formed in the AMP during this early metasomatic stage. The formation of A1-type apatite in the AMP reflects interaction of a pegmatite-derived fluid (rich in P and H_2O) with the host amphibolite further away from the contact. Textural relationships of holmquistite in both the BT zone and the endocontact (APL1, APL2 and TRN zones) also document the presence of a Li-enriched metasomatic fluid during the late stage of the metasomatic alteration.

The APL1 zone is in direct contact with the host AMP (Fig. 2). Moreover, the textural features observed in both the APL1 and the BT zones are quite similar. For this reason, the APL1 zone might be considered a strongly metasomatized former AMP, which would mean that APL1 would not be part of the endocontact but rather belong to the exocontact. This possible interpretation, however, requires further investigation. The P-rich albite in the APL2

and the TRN zones is associated with a late P-rich hydrothermal-metasomatic saccharoidal albite (albite II, for details see Kurylo et al. 2022) in proximity of the pegmatite. Therefore, the formation of the APL2 zone can be interpreted as a late stage of magmatic crystallization. A1-type apatite is texturally similar in all zones, and therefore, formed prior to the formation of the AP and TRF zones. The replacement of primary albite assemblages is evidenced by the presence of relic aplite fragments.

In contrast to other localities, where tourmaline plays an important role in buffering Ca, Mg, Fe, F, B, and Li (e.g. Černy and Burt 1984; Morgan and London 1987, 1989; Shearer et al. 1984, 1986; Martin-Izard et al. 1995; Laurs and Dilles 1996; Selway et al. 2005; Gadas et al 2023), the SLD has a low B content, and consequently, P plays the principal buffering role instead.

A1-type apatite

This apatite in the APL1 and APL2 zones points to high activities of Ca, Mn, P, and F during the early stages of metasomatism. Formation of apatite crystals can be explained by two possible mechanisms: (1) The first one assumes interaction between P, F, H_2O in the pegmatite-derived fluid and the Ca released from the plagioclase and hornblende from the host amphibolite. In this case, apatite should occur within the plagioclase rims or between plagioclase crystals; (2) The second mechanism is related to precipitation of apatite due to reaction between the P expelled from albite and the Ca derived from the amphibolite. In this case, tiny crystals of apatite should be disseminated inside the albite. This second mechanism seems to be dominant in the APL2 relics and in the TRN and PGM zones. These two precipitation mechanisms probably occurred simultaneously.

Moreover, the following two compositional trends in apatite can be distinguished (Fig. 4):

1) a gradually increasing MnO content of apatite from the BT towards APL2 zones, followed by a decrease towards the PGM. This trend most likely reflects Mn transport by a fluid that was derived from the pegmatite and buffered by triphylite.
2) a gradually decreasing F content of apatite from the BT zone to the PGM. This trend most likely reflects the F–OH exchange in the pegmatite-derived fluid, and therefore, apatite with the highest F content should be the earliest mineral phase.

A2-type apatite

Apatite chemistry. The F content of the A2-type apatite is similar to that of A1-type apatite in the APL2 relics in the AP zone. The A2-type apatite crystals contain very low amounts of trace elements, and (Mn+Fe) correlates negatively with Ca (Fig. 14). The irregular Mn and Fe distribution within the crystals is probably related to dissolution and reprecipitation of apatite during formation of the triphylite needles. The Raman spectra obtained for A2-type apatite indicate a high crystallinity.

Mobility of REEs, U, and Th in the metasomatic fluids is indicated by the presence of secondary REE -U-Th phases in A2-type apatite. On the other hand, the REE, U and Th contents of the parental pegmatite melt appear to have been low, as suggested by the absence of (REE, Th, U)-bearing minerals in the SLD pegmatites. During fluid-apatite interaction, REEs, U and Th can be leached from apatite and precipitated as secondary (REE, U, Th)-rich minerals (Pan et al. 1993a, b). In our case, however, an evaluation of such a process is complicated, because the original composition of the former apatite, i.e. the precursor to A2-type apatite, is unknown. In addition, even though REE-bearing mineral inclusions have not been found in apatite, numerous inclusions of U-rich oxides (< 1 μm) do occur, mostly intergrown with triphylite (Fig. 13). Therefore, it is feasible that actinides and perhaps also REEs were indeed leached from apatite, but only U-oxides were reprecipitated. Moreover, U-

oxides, cheralite, coffinite, and unidentified REE-Th-U phosphates occur as fine grains, which are replacing zircon and probably formed during a late stage of metasomatism.

Origin of the triphylite inclusions. The formation of triphylite needles in apatite can be explained by the two possible mechanisms.

The first mechanism could be by nucleation and growth of triphylite crystals on the apatite surface. Such a process has been inferred to explain oriented needles of rutile, ilmenite, and corundum at garnet interfaces in a metapegmatite from the Koralpe region (Eastern Alps, Austria) (Griffiths et al. 2020).

The second mechanism could be migration of Li-rich fluids through apatite (in the AP zone) and precipitation of triphylite inclusions oriented parallel to the apatite *c*-axis or along apatite nanochannels. Such a mechanism was investigated experimentally with Durango fluorapatite, which involved HCl and H_2SO_4 solutions (Harlov et al. 2005); the experimental results documented that apatite was pervasively penetrated by reaction fronts during dissolution-precipitation. Moreover, Harlov et al. (2005) observed monazite inclusions, which were formed in the reacted areas characterized by depletion in trace elements. A similar process was also inferred for natural apatites from different localities (e.g. Harlov et al. 2002; Ziemann et al. 2005; Pan et al. 1993).

In contrast to the observations described by Harlov et al. (2005), no relationship between F content in apatite and the presence of triphylite inclusions was observed. Nevertheless, areas with a high density of triphylite needles in the host apatite clearly correlate spatially with areas that exhibit lower MnO contents. In addition, individual triphylite crystals occurring in the interstitial space between different apatite grains display compositions that are similar to those of the triphylite needles within apatite. Such textural and compositional relationships may point to a direct reaction of a Li-rich fluid with the apatite surface during triphylite nucleation and growth. This mechanism can also be supported by the common intergrowths of

447 triphylite rods with ilmenite and cassiterite, which are typical in the albite relics. Partial
448 dissolution and reprecipitation of the host apatite during metasomatic alteration was most
449 likely coupled with leaching of Mn and Fe from the apatite structure, consistent with the
450 features observed in X-ray elemental maps and EMP cross-section analyses (Fig. 6). Further
451 growth of the triphylite needles was facilitated by fluids in nanochannels along the *c*-axis
452 and/or nanoporosity of apatite. This interpretation is comparable with those used to explain
453 similar features in other apatite occurrences, for example, oriented inclusions of monazite
454 (Pan et al. 1993; Harlov et al. 2005) or pyrrhotite (Broska et al. 2012). However, triphylite
455 inclusions and interstitial triphylite have higher Mn contents, lower Fe/(Fe+Mn) values, and
456 lower MgO contents compared to triphylite from the TR and TRN zones. Prismatic triphylite
457 inclusions in apatite, which exhibit random orientations, were not nucleated in direct contact
458 (or only partial contact) with apatite, but were more likely trapped during subsequent apatite
459 growth, as shown by the experiments with Durango apatite (Harlov et al. 2005).
460
461 **A3-type apatite**
462 The late metasomatic A3-type apatite is rich in OH^-, Cl, CO_2, and locally S, but poor in
463 F. The presence of CO_2 in the apatite structure was confirmed by Raman spectroscopy. Curve
464 fitting of the Raman spectrum obtained from a carbon-rich A3-type apatite (1.7 wt% CO_2;
465 Table 4, analysis 12) in the 1060–1090 cm^{-1} region yields three Gaussian peaks at ~1070,
466 1072.5, and ~1076 cm^{-1} (Fig. 9c). The band at 1070 cm^{-1} (ν_1) documents the presence of
467 CO_3^{2-} in the apatite structure (Penel et al. 1998; Antonakos et al. 2007; Awonusi et al. 2007).
468 On the other hand, the ν_1 vibration modes reflecting CO_3^{2-} were not observed in the A1- and
469 A2-type apatites. The increased role of carbon during the late stage of metasomatic alteration
470 is also documented by the dense network of secondary fluid inclusions of CO_2 and CO in the
471 A2-type apatite, and by the presence of siderite associated with A3-type apatite veinlets.

Thus, the volatile components of the metasomatic fluid evolved in the following temporal sequence: HF – OH – (HCl, HS^-, CO, CO_2, N_2).

Triphylite chemistry

Triphylite is a common mineral in the SLD, and its composition was discussed previously in Kurylo et al. (2022). The observed decrease in the Fe/(Mn+Fe) value with time is related to fractionation of the pegmatite melt (Fransolet et al. 1986; Roda et al. 2004; Baijot et al. 2012). Triphylite in the main pegmatite displays a similar Fe/(Fe+Mn) value and Mg content as in triphylite that commonly occurs in other Li-bearing pegmatite dikes of the SLD (Kurylo et al. 2022). However, its Mg content (up to 2.1 wt%) is approximately half that of triphylite from the contact zone, pointing to a relatively high degree of contamination from the host amphibolite, even at a distance from the actual AMP / PGM contact.

Triphylites in the TR and TRN zones show an Fe/(Fe+Mn) value that is similar to the one observed in triphylite in the adjacent pegmatite, but they have a higher Mg content (~ 4.5wt%), which probably reflects a significantly higher degree of contamination from the host amphibolite. In the AP zone, both the triphylite inclusions in A2-type apatite and the interstitial triphylite follow a common trend with the triphylite in the TR and TRN zones (Fig. 11). This trend displays a gradual decrease in Fe and Mg contents in the triphylite from the TR and the TRN zones towards the triphylite inclusions in A2-type apatite, and thus, indicates that the triphylite inclusions are the latest triphylite variety to crystallize.

Origin of metasomatic fluid

Almost all former granite pegmatites in the SLD, including the pegmatite studied here, are compositionally similar: they are peraluminous, very poor in mafic components, undersaturated in F, B and H_2O, but saturated in Li and P, as reflected by the high abundance

of petalite, spodumene, montebrasite, triphylite, and P-rich feldspars (Eremenko et a1. 1996; Kurylo et al. 2022; Syomka et al. 2023). No assemblages containing F-rich minerals were detected in the adjacent pegmatite dike, except for apatite and biotite in the contact zone (Ivanov et al. 2011). Therefore, the F content of the parental melt must have been low, but our observations suggest that the role of F in the residual melt and in the associated metasomatic fluid, i.e., near the end of magmatic crystallisation, was more pronounced, finally leading to the formation of fluorapatite and F-rich biotite in the contact zone. The residual melt was also rich in incompatible elements (e.g., Na, Li, Rb, P, Nb, Ta, Sn), and subsequently crystallized saccharoidal albite-rich domains in proximity of the host amphibolite. Detailed analysis of the studied contact zone indicates that K, Na, Li, Rb, F, P, and possibly Mn were partially transferred to the metasomatic fluid and transported to the host amphibolite, forming new mineral assemblages at the amphibolite / pegmatite contact.

Metasomatic/hydrothermal stages

Based on the observations reported in this study, two stages of the metasomatic alteration can be distinguished at the pegmatite/amphibolite contact. The first metasomatic stage consisted of a K-Rb-F metasomatism at relatively low P activity, whereas the second involved a fluid with high activity of Li and P. Moreover, the transition from the first to the second stage was gradual. The characteristic minerals of the first metasomatic stage are biotite and A1-type apatite, whereas the second stage is characterized by A2-type apatite, triphylite, and holmquistite. Finally, A3-type apatite represents a late metasomatic alteration of mainly triphylite and zircon.

Alteration of hornblende and plagioclase in the amphibolite host rock by the pegmatite-derived fluid released Ca, Fe, and Mg, which were transported back to the pegmatite, probably along fractures. The interaction of Ca, Fe, and Mg with P, Li, F, and Mn led to the

formation of A2-type apatite and triphylite. This newly formed A2-type apatite was able to inhibit considerably the migration of Li from the pegmatite towards the host amphibolite, thus acting like a geochemical barrier. Such a scenario could also explain the formation of the TR zone and its location between the PGM and the AP zone. The TR zone has probably been developed from the former pegmatite mineral assemblage, as indicated by the numerous relics of albite within it (Figs. 2, 10a). (Fig. 2). Greenish-blue A1-type apatite armored Li from the Li-rich pegmatite fluid and significantly reduced the Li mobility in the contact zone.

CONCLUSIONS

In the Stankuvatske Li deposit (Ukrainian shield), the interaction of a pegmatite-derived fluid (rich in K, Na, Li, Rb, F, P, and Mn) with the host amphibolite led to the formation of an exocontact in the host amphibolite. During of this alteration, the removal of Ca, Fe and Mg from the amphibolite and their transport towards the pegmatite caused an interaction with the pegmatite-derived metasomatic fluid, resulting in the formation of the pegmatite endocontact, which contains several mineral zones, including the TR and the AP zones. The partial escape of Li to the country rock is documented by the presence of holmquistite in the exocontact. The AP zone not only witnesses the migration of the Li-rich fluid, but also significantly inhibited Li migration into the host amphibolite. Late Li-rich fluids infiltrated into the apatite zone, where they reacted with the apatite surface to produce the triphylite inclusions that are oriented along the structural *c*-axis nanochannels of the A2-type apatite. Metasomatic processes in the SLD, thus, can be viewed as an example of the formation of apatite, which then acts as a geochemical barrier, with metallogenic implications.

IMPLICATIONS

The described function of apatite as a geochemical barrier might have been responsible for the accumulation of important rare metals (Li, Rb, Cs, Nb, Ta, and Sn) in the endocontact of the pegmatite in the Stankuvatske Li-ore deposit. Therefore, the presence of an apatite zone at the contact with the host rock might be used as a prospecting tool for rare metals in other pegmatites around the world. The apatite barrier described here also reiterates the importance of this mineral in dissolution-reprecipitation processes during metasomatic fluid infiltration. The proposed role of apatite as a geochemical barrier can be further supported in other circumstances, for example, by preserved monazite and xenotime relics surrounded by a tiny apatite corona, as reported from various localities worldwide (e.g., see Finger et al. 1998; Hentschel et al., 2020). In these latter cases, the apatite barrier was formed through alteration of monazite / xenotime, thus preventing further monazite / xenotime dissolution.

ACKNOWLEDGEMENTS

The authors are grateful for the financial support provided by the PEGMAT grant within the ERA MIN2 framework. We are grateful to J. Luptakova and S. Milovská for their help in operating the Raman spectrometer and to S. Georgiev for his assistance at the LA-ICP-MS and CL-luminescence works. We are also very grateful for the invaluable comments from three anonymous reviewers.

REFERENCES CITED

Antonakos, A., Liarokapis, E., and Leventouri, T. (2007) Micro-Raman and FTIR studies of synthetic and natural apatites. Biomaterials, 28(19), 3043–3054. https://doi.org/10.1016/j.biomaterials.2007.02.028

Awonusi, A., Morris, M. D., and Tecklenburg, M. M. J. (2007) Carbonate assignment and calibration in the Raman spectrum of apatite. Calcified Tissue International, 81(1), 46–52. https://doi.org/10.1007/s00223-007-9034-0

572 Baijot, M., Hatert, F., and Philippo, S. (2012) Mineralogy and geochemistry OF phosphates
573 and silicates in the Sapucaia pegmatite, Minas Gerais, Brazil: Genetic implications.
574 Canadian Mineralogist, 50 (6), 1531–1554. https://doi.org/10.3749/canmin.50.6.1531
575 Broska, I., Krogh Ravna, E.J., Vojtko, P., Janák, M., Konečný, P., Pentrák, M., Bačík, P.,
576 Luptáková, J., and Kullerud, K. (2014) Oriented inclusions in apatite in a post-UHP fluid-
577 mediated regime (Tromsø Nappe, Norway). European Journal of Mineralogy, 26(5), 623–
578 634. http://doi.org/10.1127/0935-1221/2014/0026-2396.
579 Černý, P., and Burt, D.M. (1984) Paragenesis, crystallochemical characteristics, and
580 geochemical evolution of micas in granite pegmatites. In S.W. Bailey, Ed., Micas.
581 Mineralogical Society of America, Review in Mineralogy, 13, 257–298.
582 http://doi.org/10.1515/9781501508820-012.
583 Černý, P., and Ercit, T.S. (2005) The classification of granitic pegmatites revisited. Canadian
584 Mineralogist, 43(6), 2005–2026. https://doi.org/10.2113/gscanmin.43.6.2005.
585 Eremenko H.K., Ivanov B.N. Belykh N.A., Kuzmenko A.V. and Makyvchuk O.F. (1996)
586 Mineralogical features and conditions of formation of lithium pegmatites of Kirovograd
587 block (Ukrainian Shield). Mineralohichnyi zhurnal, 18, 48–57 (in Russian).
588 Finger, F., Broska, I., Roberts, M.P., and Schermaier, A. (1998) Replacement of primary
589 monazite by apatite-allanite-epidote coronas in an amphibolite facies granite gneiss from
590 the eastern Alps. American Mineralogist, 83(3–4), 248–258, http://doi.org/10.2138/am-
591 1998-3-408.
592 Fransolet, A. M. (2007) Phosphate associations in the granitic pegmatites : the relevant
593 significance of these accessory minerals. 3th PEG, 5(May), 5–6.
594 Frost, R. L., Xi, Y., Scholz, R., López, A., Belotti, F. M., and Chaves, M. L. S. C. (2013)
595 Raman and infrared spectroscopic characterization of the phosphate mineral lithiophilite -

596 $LiMnPO_4$. Phosphorus, Sulfur and Silicon and the Related Elements, 188, 1526–1534.
597 https://doi.org/10.1080/10426507.2012.761985

598 Gadas, P., Novák, M., Galiová, M. V., and Pezzotta, F. (2023) Chemical composition of
599 tourmalines from the Manjaka pegmatite and its exocontact, Sahatany Valley,
600 Madagascar. Journal of Geosciences (Czech Republic), 68 (3), 185–202.
601 https://doi.org/10.3190/jgeosci.374

602 Griffiths, T.A., Habler, G., and Abart R. (2020) Determining the origin of inclusions in
603 garnet: challenges and new diagnostic criteria. American journal of science, 320, 753–
604 789.

605 Guillong, M., Meier, D. L., Allan, M., Heinrich, C. and Yardley, B. (2008) SILLS: a Matlab-
606 based program for reduction of laser ablation ICPMS data of homogeneous materials and
607 inclusions. In: Sylvester P. (ed.). Laser-Ablation-ICP-MS in the earth sciences, current
608 practices and outstanding issues. Vancouver: Mineralogical Association of Canada Short
609 Course, 328–222.

610 Harlov, D.E., Andersson, U.B., Förster, H.-J., Nyström, J.O., Dulski, P., and Broman, C.
611 (2002) Apatite-monazite relations in the Kiirunavaara magnetite-apatite ore, northern
612 Sweden. Chemical Geology, 191, 47–72. http://doi.org/10.1016/S0009-2541(02)00148-1.

613 Harlov, D.E., Wirth, R., and Förster, H.J. (2005) An experimental study of dissolution-
614 reprecipitation in fluorapatite: Fluid infiltration and the formation of monazite.
615 Contributions to Mineralogy and Petrology, 150 (3), 268–286.
616 http://doi.org/10.1007/s00410-005-0017-8.

617 Harlov, D.E., and Foster, H.-J. (2002) High-Grade Fluid Metasomatism on both a Local and a
618 Regional Scale: the Seward Peninsula, Alaska, and the Val Strona di Omegna, Ivrea-
619 Verbano Zone, Northern Italy. Part I: Petrography and Silicate Mineral Chemistry.
620 Journal of petrology, 43, 769–799. http://doi.org/10.1093/petrology/43.5.769.

Hentschel, F., Janots, E., Trepmann, C.A., Magnin, V., and Lanari, P. (2020) Corona formation around monazite and xenotime during greenschist-facies metamorphism and deformation. European Journal of Mineralogy, 32, 521–544. http://doi.org/10.5194/ejm-32-521-2020.

Hrinchenko, O., Bondarenko, S., Syomka, V., Ivanov, B.N., and Kanunikova L.I. (2016) Composition of Ta-Nb minerals in pegmatites and apogranite metasomatites from Shpoliano-Tashlyk ore region. Heokhimiia i rudoutvorennia, 36, 47–57. https://doi.org/10.15407/gof.2016.36.047 (in Ukrainian).

Ivanov, B., and Lysenko, V. (2001) Results of exploration works on lithium and gold in the years 1991–2001, with estimation of reserves on square of 10Kat0 square km in frame of Lypniazhka Dome Structure. Geological report, KP "Kirovgeology", Smolino (in Russian).

Ivanov, B.N., Kosiuga, V.N., and Pogukai, V.I. (2011) Areal end exocontact metasomatites of Shpoliano-Tashlyk ore region. Heokhimiia i rudoutvorennia, 30, 10–17 (in Russian).

Kato, S., Ikeda, S., Saito, K., and Ogasawara, M. (2018) Fe incorporation into hydroxyapatite channels by Fe loading and post-annealing. Journal of Solid State Chemistry, 265, 411–416. https://doi.org/10.1016/j.jssc.2018.06.032.

Kurylo, S., Uher, P., Broska, I., Lyzhachenko, N., Bondarenko, S., and Gieré, R. (2022) Fine-grained petalite and spodumene dykes in the Stankuvatske Li-deposit, Ukrainian Shield: products of tectono–metamorphic recrystallisation. Mineralogical Magazine, 86, 863–882. https://doi.org/10.1180/mgm.2022.100.

Laurs, B. M., and Dilles, J. H. (1996). Emerald mineralization and metasomatism of amphibolite, khaltaro granitic pegmatite-Hydrothermal vein system, Haramosh Mountains, Northern Pakistan. The Canadian Mineralogist, 34, 1253–1286. https://www.researchgate.net/publication/279652732

Martin-Izard, A., Paniagua, A., Moreiras, D., Acevedo, R. D., and Marcos-Pascual, C. (1995) Metasomatism at a granitic pegmatite - Dunite contact in Galicia: The Franqueira occurrence of chrysoberyl (alexandrite), emerald, and phenakite. Canadian Mineralogist, 33, 775–792.

Morgan, G.B. VI, and London, D. (1987) Alteration of amphibolitic wallrocks around the Tanco rare-element pegmatite, Bernic Lake, Manitoba. American Mineralogist, 72, 1097–1121.

Morgan, G. B., and London, D. (1989). Experimental reactions of amphibolite with boron-bearing aqueous fluids at 200 MPa: implications for tourmaline stability and partial melting in mafic rocks. Contributions to Mineralogy and Petrology, 102(3), 281–297. https://doi.org/10.1007/BF00373721

Nechaev, S.V., Makivchuk, O.F. and Belykh, N.A. (1991) New rare-metal ore region of Ukraine. Heolohichnyi zhurnal, 4, 119–123 (in Ukrainian).

Pan, Y., Fleet, M.E., and Macrae, N.D. (1993a) Oriented monazite inclusions in apatite porphyroblasts from the Hemlo gold deposit, Ontario, Canada. Mineralogical Magazine, 57, 697–707. https://doi.org/10.1180/minmag.1993.057.389.14.

Pan, Y., Fleet, M.E., and Macrae, N.D. (1993b) Late alteration in titanite (CaTiSiOS): Redistribution and remobilization of rare earth elements and implications for U / Pb and Th / Pb geochronology and nuclear waste disposal. Geochimica a Cosmochimica Acta, 51, 355–367.

Pearce, N. J. G., Perkins, W. T., Westgate, J. A., Gorton, M. P., Jackson, S. E., Neal, C. R. and Chenery, S. P. (1997) A compilation of new and published major and trace element data for NIST SRM 610 and NIST SRM 612 glass reference materials. The journal of Geostandards Newsletter, 21, 115–144. https://doi.org/10.1111/j.1751-908X.1997.tb00538.x

671 Penel, G., Leroy, G., Rey, C., and Bres, E. (1998) Laboratory Investigations MicroRaman
672 Spectral Study of the PO_4 and CO_3 Vibrational Modes in Synthetic and Biological
673 Apatites. Calcified Tissue International, 63, 475–481.
674 Roda, E., Pesquera, A., Fontan, F., and Keller, P. (2004) Phosphate mineral associations in the
675 Cañada pegmatite (Salamanca, Spain): Paragenetic relationships, chemical compositions,
676 and implications for pegmatite evolution. American Mineralogist, 89, 110–125.
677 Selway, J. B., Breaks, F. W., and Tindle, A. G. (2005) A Review of Rare-Element (Li-Cs-Ta)
678 Pegmatite Exploration Techniques for the Superior Province, Canada, and Large
679 Worldwide Tantalum Deposits. Exploration and Mining Geology, 14, 1–30.
680 Shearer, C.K., Papike, J.J., Simon, S.B., and Laul, J.C. (1986) Pegmatite-wall-rock
681 interactions, Black Hills, South Dakota: interaction between pegmatite-derived fluids and
682 quartz-mica schist wall-rock. American Mineralogist, 71 (3–4), 518–539.
683 Shearer, C.K., Papike, J.J., Simon, S.B., Laul, J.C., and Christian, R.P. (1984)
684 Pegmatite/wallrock interactions, Black Hills, South Dakota: Progressive boron
685 metasomatism adjacent to the Tip Top pegmatite. Geochimica et Cosmochimica Acta,
686 48(12), 2563–2579. https://doi.org/10.1016/0016-7037(84)90306-5
687 Shcherbak, N.P., Artemenko, G.V., Lisna, I.M., Ponomarenko A.N., and Shumlianskyi L.V.
688 (2008) Geochronology of Early Precambrian of Ukrainian Shield. Proterozoi, 239 p.
689 Naukova Dumka, Kyiv, Ukraine.
690 Stepanyuk, L.M., Hrinchenko, O.V., Bondarenko, S.M., Syomka, V.O., and Kurylo, S.I.
691 (2018) Geochronology of lithium-bearing granitoids of Inhul Megablock (Ukrainian
692 Shield). Visnyk Kyivskoho natsionalnoho universytetu imeni Tarasa Shevchenka. Seriia
693 Heolohiia, 3, 23–28, https://doi.org/10.17721/1728-2713.82.03, (in Ukrainian).
694 Stepanyuk, L., Kurylo, S., Syomka, V., Dovbush, T., Bondarenko, S., Kovtun, O., Kotvitska,
695 I. (2021) Uranium-lead geochronology on monazite from the granite of the Lypnyazka

massif and its framing (Ingul Domain of the Ukrainian Shield). Heokhimiia i rudoutvorennia, 42, 71–79 (in Ukrainian). https://doi.org/10.15407/gof.2021.42.071.

Stormer, J.C., Milton, J., Pierson, M.L., and Tacker, R.C. (1993) Variation of F and Cl X-ray intensity due to abisotropic diffusion in apatite during electron microprobe analyses. American mineralogist, 78, 641–648.

Syomka, V.O., Ponomarenko, O.M., Stepanyuk, L.M., Bondarenko, S.M., Sukach, V.V., Kurylo, S.I., and Donskyi, M.O. (2022) Lithium ores of Stankuvatka and Polokhivka ore fields (Ukrainian Shield). Mineralogical Journal, 44(4), 102–124. https://doi.org/10.15407/mineraljournal.44.04.102.

Sherbakov, I. (2005) Petrology of Ukrainian Shield, 366 p. ZUKC, Lviv.

Vozniak, D.K. and Pavlyshyn, V.I. (2001) The high thermobaric flow of liquid CO2 and it role in mineralisation (in example of Ukrainian Shield). Mineralohichnyi zhurnal, 23, 12–18 (in Ukrainian).

Vozniak, D.K., Bugaenko, V.M., Galaburdam Ju.A., Melnikov, V.S., Pavlyshyn, V.I., Bondarenko, S.M. and Syomka, V.O. (2000) Features of mineral composition and conditions of formation of rare-metal pegmatites on the west part of Kirovohrad block (Ukrainian Shield). Mineralohichnyi zhurnal, 22, 21–41 (in Ukrainian).

Warr, L.N. (2021) IMA-CNMNC approved mineral symbols. Mineralogical Magazine, 85, 291–320.

Yesypchuk, K., Bobrov, O., Stepaniyuk, L. (2004) Correlation chronostratigraphic scheme of the Early Precambrian of the Ukrainian, 30 p. UkrDGRI, Kyiv.

Zhang, R.Y., and Liou, J.G. (1999) Exsolution lamellae in minerals from ultrahigh-pressure rocks. International Geology Review, 41(11), 981–993. https://doi.org/10.1080/00206819909465184.

Zhu, Y., and Massonne, H.J. (2005) Discovery of pyrrhotite exsolution in apatite. Acta Petrologia Sinica, 2, 405–410.

Ziemann, M.A., Förster, H.-J., Harlov, D.E., and Frei, D. (2005) Origin of fluorapatite-monazite assemblages in a metamorphosed, sillimanitebearing pegmatoid, Reinbolt Hills, East Antarctica. European Journal of Mineralogy, 17(4), 567–580. https://doi.org/10.1127/0935-1221/2005/0017-0567.

List of figure captions

FIGURE 1. Geological maps of the study area in Ukraine. (**a**) Map showing the regional geology of the western Inhul Domain. (**b**) Simplified geological map (Ivanov and Lysenko, 2001) displaying the locations of the rare-element pegmatite dikes (Ta-Nb- and Li-bearing) and the places where samples were collected (LP: Lypniazhka Dome Structure).

FIGURE 2. Contact between amphibolite host rock (left) and pegmatite dike (right), exhibiting mineralogically well-defined zones (sample 61-89/240.5 m). (**a**) Polished hand specimen. (**b**) Thin section viewed under an optical microscope in plane-polarized light. The direct contact with the amphibolite is represented by the biotite zone (BT) in the exocontact. In the endocontact, there are distinct zones formed by a fluid from / towards the contact with amphibolite; these zones are abbreviated as follows: APL – Aplitic (APL1: quartz + plagioclase + apatite + niobian rutile; APL2: albite + apatite + niobian rutile; APL2 (relics): albite / apatite relics in the Apatite and Triphylite zones); AP – Apatite; TR – Triphylite; TRN – Transitional, adjacent to the spodumene-petalite-bearing pegmatite (PGM).

FIGURE 3. Photomicrographs of the apatite types from the different mineral zones (plane-polarized light): (**a**) A1-type apatite in the host amphibolite (sample 61-89/ 236 m); (**b**) Apatite included in biotite from the matrix of the BT zone; (**c**) Elongated crystals of apatite in albite (AP zone); apatite occurs at the grain boundaries and as secondary needles in albite; (**d**) Apatite included in an albite relic, enclosed in the triphylite cluster (APL2 zone). Photomicrographs (**b** – **d**) – sample 61-89/240.5 m.

FIGURE 4. X_F values (a) and MnO contents (b) in the different types of apatite plotted along increasing distance from the amphibolite (AMP) towards the pegmatite dike (PGM), sample 61-89/240.5 m and 61-89/241.5 m. For abbreviations on x axis, please see Table 1. All apatite analyses used for plotting these graphs are listed in the Supplementary Material (Tables S2A and S2B).

FIGURE 5. Apatite type A2 from the Stankuvatske Li-pegmatite field. (**a**) Triphylite rods in apatite (plane-polarized light; arrows point to triphylite inclusions oriented along c-axis of apatite (AP zone; sample 61-89/240.5 m). (**b**) greenish-blue apatite displaying yellow cathodoluminescence (AP zone; sample 61-89/240.5 m). (**c**) Green apatite crystal liberated from drill core (sample 34-91/113–114 m); it shows an irregular shape due to the exposure to corrosive F-rich fluids. (**d**) Plane-polarized light image of apatite with needles of oriented triphylite (sample 34-91/113-114 m).

FIGURE 6. Manganese- and iron-distribution in A2-type apatite. (**a**) High-contrast BSE image of A2-type apatite, and X-ray element maps of Mn (**b**) and Fe (**c**) for the same apatite grain. EPM cross-sections displaying MnO (wt%) and X_F variation in apatite, from different parts of the Apatite zone: (**d**) Compositional variation across the apatite along the A-B profile shown in (a), apatite is at the contact with Aplite zone (APL2); (**e**) Apatite from the central part of the Apatite zone; (**d**) Apatite from the contact between the Apatite and Triphylite zones. All apatite analyses used for plotting these graphs are listed in the Supplementary Material (Table S2B).

FIGURE 7. Photomicrographs of apatite type A2 with triphylite and fluid inclusions (plane-polarized light; sample 61-89/240 m), documented by the Raman spectra: (**a**) Crystallographically oriented triphylite needles in apatite from the apatite zone (sample 61-89/240.5 m); (**b**) The peak at 951 cm^{-1} is evidence for triphylite, whereas the peak at 964 cm^{-1} points to host apatite; (**c**) Species identification in fluid inclusions in apatite.

FIGURE 8. Late-hydrothermal A3-type apatite (sample 61-89/240.5 m). (**a**) network of A3-type apatite displaying yellow cathodoluminescence; (**b**) BSE image of compositionally zoned apatite, locally associated with carbonate (**c**).

FIGURE 9. Raman spectra of apatite occurring in the endocontact (sample 61-89/240.5 m). (**a**) Background-subtracted spectra of A1- , A2-, and A3-type apatites; (**b**) Enlarged Raman spectra of the carbonate ν_1 and phosphate ν_3 mode regions. (**c**) Raman spectra in the CO_3^{2-} and PO_4^{3-} regions with

774 fitted Gaussian peaks revealing the presence of CO_2 at ~ 1070 cm^{-1} in the A3-type apatite (1.7 wt% of
775 CO_2).

776 *Abbreviations:* AP– apatite zone; APL1 – aplitic zone (plagioclase–quartz); ⊥ *c* – crystal orientation
777 perpendicular to *c*-axis in apatite; II *c* – parallel to *c*-axis.

778 *Notes:* A1-type apatite was analyzed only ⊥ *c*, because the II *c* sections were not found; the crystal
779 orientation of A3-type apatite is not detectable. * – most intense Raman peak of the resin used for
780 sample preparation.

781 **FIGURE 10.** Triphylite from the Triphylite zone (TR) (sample 61-89/240.5 m). (**a**) Photomicrograph
782 shows a cluster of triphylite crystals; relics of albite enclosed in the triphylite cluster (cross-polarized
783 light); (**b**) BSE image showing zoning in triphylite; (**c**) Photomicrograph of triphylite associated with
784 albite from the transitional (TRN) zone (plane-polarized light); (**d**) BSE image displaying triphylite
785 from the TRN zone partially replaced by Cl-rich A3-type apatite and pyrrhotite.

786 **FIGURE 11.** Composition of triphylites from the different mineral zones, including the triphylite
787 inclusions in A2-type apatite (marked by the black crosses). Field a: chemical variety of triphylite in
788 the petalite- and spodumene-metapegmatite dikes. Field b: triphylite in small metapegmatite dikes
789 with a high degree of contamination from the host amphibolite. Two distinct trends are seen for
790 triphylite from the Li-bearing dikes (1) and from the endocontact zone (2). All triphylite analyses used
791 for plotting this graph are listed in the Supplementary Material (Table S3).

792 **FIGURE 12.** Raman spectra of triphylite from the triphylite (TR) zone (gr1 and gr2 are two separate
793 grains), the transitional (TRN) zone, and the adjacent pegmatite (PGM, sample 61-89 / 241.5 m).

794 **FIGURE 13.** Triphylite from the Apatite zone (sample 61-89 /240.5m). **(a)** Apatite type A2 containing
795 oriented triphylite rods; labels display locations of triphylite grains shown in (**b**–**i**): (**b** and **c**)
796 interstitial triphylite grains occurring along apatite contacts; (**d**) Triphylite needle associated with U-
797 oxides; (**e**) Fe-oxide and triphylite intergrowth; (**f**): Triphylite intergrown with Fe-oxide and U-oxide;
798 (**g**) Triphylite associated with columbite, ilmenite and U-oxides; (**h**) Triphylite associated with U-Th-
799 Pb–oxides, cassiterite, and Fe-oxide; (**i**): Triphylite relic after replacement by apatite, associated with
800 pyrrhotite, galena, and U-Th-Pb-oxides.

Mineral abbreviations: trp – triphylite; Ap – apatite; ilm – ilmenite; clm – columbite; cas – cassiterite; U-ox – uranium oxide; U-Th-Pb – uranium-thorium-lead oxides; gal – galena; po – pyrrhotite.

FIGURE 14. Plot of Ca (apfu) *vs.* (Mn+Fe) (apfu) in A2-type apatite (for legend, see Table 1). All apatite analyses used for plotting this graph are listed in the Supplementary Material (Tables S2A and S2B).

This is the peer-reviewed, final accepted version for American Mineralogist, published by the Mineralogical Society of America.
The published version is subject to change. Cite as Authors (Year) Title. American Mineralogist, in press.
DOI: https://doi.org/10.2138/am-2023-9172. http://www.minsocam.org/

TABLE 1. Samples, mineral zones, and apatite types investigated in thin sections and mineral concentrates.

Sample	Zone	Abbreviation	Apatite type
Host rock			
61-89/235 m	Amphibolite	AMP	A1
Contact between amphibolite and Li-bearing pegmatite			
61-89/240.5 m	*Exocontact*		
	Biotite zone (Bt + Pl + Qz + Hlm)	BT	A1
	Endocontact		
	Aplite (Ab + Qz + Ap+ Rt)	APL1	A1
	Aplite (Ab + Ap + Rt)	APL2	A1
	Aplite relics (Ab + Ap ± Rt)	APL2	A1
	Apatite zone	AP	A2, A3
	Triphylite zone	TR	A3
	Transitional zone	TRN	A1, A3
	Adjacent Ptl–Spd pegmatite	PGM	A1, A3
Li-bearing dikes			
61-89/241.5 m	Adjacent Pt–Spd pegmatite	PGM	A1, A3
77-90/242 m	Spd pegmatite dike	PGM	A2
Mineral concentrates*			
34-91/109.5-110.6 m	Biotite exocontact zone	APM1	A2
34-91/113-114 m	Li-bearing pegmatite	APM2	A2
34-92/114-116 m	Biotite exocontact zone	APM3	A2

Notes. Mineral abbreviations according to Warr (2021).
*concentrates of grains APM1, APM2, and APM3 are mono-fractions liberated from drill core materials.

This is the peer-reviewed, final accepted version for American Mineralogist, published by the Mineralogical Society of America.
The published version is subject to change. Cite as Authors (Year) Title. American Mineralogist, in press.
DOI: https://doi.org/10.2138/am-2023-9172. http://www.minsocam.org/

TABLE 2. Analytical conditions of the elements detected by EMP in apatite and triphylite.

Element	X-ray Line	Crystal	Standard	Detection limit (ppm)*
Apatite				
Ca	Kα	PETL	Apatite	76
U	Mβ	PETL	UO_2	148
Th	Mα	PETL	ThO_2	110
Cl	Kα	PETL	Tugtupite	35
P	Kα	PETL	Apatite	188
S	Kα	PETL	Barite	65
Pb	Mα	PETL	Crocoite	250
Y	Lα	PETL	YPO_4	58
F	Kα	LDE1	Fluorite	400
Sr	Lα	TAP	Celestite	129
Na	Kα	TAP	Albite	70
Si	Kα	TAP	Albite	76
Mg	Kα	TAP	Diopside	58
Fe	Kα	LIF	Hematite	158
Mn	Kα	LIF	Rhodonite	170
Ti	Kα	LIF	Rutile	473
La	Lα	LIFH	$LaPO_4$	186
Ce	Lα	LIFH	$CePO_4$	164
Pr	Lβ	LIFH	$PrPO_4$	163
Nd	Lα	LIFH	$NdPO_5$	300
Sm	Lα	LIFH	$CePO_4$	164
Triphylite				
Ca	Kα	PETL	Diopside	80
P	Kα	PETL	Apatite	160
Sr	Lα	TAP	Celestite	570
Si	Kα	TAP	Albite	385
Al	Kα	TAP	Albite	255
Na	Kα	TAP	Albite	240
Mg	Kα	TAP	Diopside	150
Zn	Kα	LIF	Gahnite	675
Fe	Kα	LIF	Hematite	420
Mn	Kα	LIF	Rhodonite	450

*based on 3σ.

This is the peer-reviewed, final accepted version for American Mineralogist, published by the Mineralogical Society of America.
The published version is subject to change. Cite as Authors (Year) Title. American Mineralogist, in press.
DOI: https://doi.org/10.2138/am-2023-9172. http://www.minsocam.org/

TABLE 3. Summary of petrographic and compositional features of different types of apatite.*

Zone/ type	Abun-dance	Phosphate texture	Size	X^{Ap}_{FAp} (average)	MnO (wt%)	FeO (wt%)	Mn/Fe (at. ratio)
A1-type apatite							
AMP	x	Euhedral, prismatic	<50 μm	0.4-0.55 (0.49)	0.02	0.35	0.08
BT	x	Euhedral prismatic, long-prismatic	<50 μm	0.71–0.94 (0.80)	0.06	0.24	0.35
APL1	xxx	Euhedral, prismatic, long-prismatic, needle-shaped	10-200 μm	0.64–0.91 (0.66)	0.1	0.16	2.5
APL2	xxx	Euhedral, long-prismatic, needle-shaped	<50 μm	0.61-0.69 (0.65)	1.25	0.26	5.7
TR	xx	Euhedral and subhedral prismatic, long-prismatic	20-100 μm	0.4-0.56 (0.48)	0.67	0.12	6.4
PGM	x	Euhedral and subhedral prismatic, long-prismatic	20-100 μm	0.21	0.53	0.03	20
A2-type apatite with triphylite inclusions							
AP	xxx	Euhedral and subhedral, with triphylite inclusions,	1.0-2.5 mm	0.62-0.64	1.05	0.13	8.8
APM1				0.58-0.72	1.21	0.16	7.6
APM2		Mineral concentrates	up to 3 mm	0.65-0.78	0.48	0.17	3.09
APM3				0.61-0.73	1.23	0.13	10.8
A3-type apatite							
AP, TR, TRN, PGM		irregular veins, anhedral, replacing texture	<10 μm	<0.02	0.7-1.62	1.4-2.1	0.2-1.1

* Notes: Abbreviations for mineral zones and apatite types are given in Table 1.

This is the peer-reviewed, final accepted version for American Mineralogist, published by the Mineralogical Society of America.
The published version is subject to change. Cite as Authors (Year) Title. American Mineralogist, in press.
DOI: https://doi.org/10.2138/am-2023-9172. http://www.minsocam.org/

TABLE 4. Representative EMP analyses (in wt%) of apatite.*

	A-1 type apatite									A3-type apatite		
Zones/type	**BT**		**APL1**		**APL2****			**PGM**		**TR**	**TRN**	**TRN**
Analysis No.	1	2	3	4	5	6	7	8	9	10	11	12
SO_3	0.01	bdl	bdl	bdl	0.01	bdl	bdl	0.02	bdl	0.01	0.54	0.0
P_2O_5	41.89	41.77	42.50	42.20	42.61	42.28	42.45	42.56	42.53	40.13	38.79	38.6
SiO_2	0.18	0.22	0.09	0.04	0.04	0.12	0.09	0.24	0.19	bdl	bdl	0.16
Al_2O_3	0.02	0.03	0.03	0.02	0.02	0.01	0.04	0.04	0.02	bdl	bdl	bdl
Y_2O_3	0.03	0.13	0.05	0.05	bdl	0.06	bdl	0.03	0.02	0.09	0.02	bdl
La_2O_3	0.07	bdl	bdl	0.05	bdl	bdl	0.03	bdl	bdl	na	na	na
Ce_2O_3	bdl	0.06	0.03	0.03	0.06	bdl	0.13	bdl	bdl	bdl	0.06	bdl
Pr_2O_3	bdl	bdl	bdl	0.03	0.03	0.08	0.04	bdl	bdl	na	na	na
Nd_2O_3	0.05	0.07	0.05	bdl	0.06	0.03	bdl	bdl	bdl	na	na	na
Sm_2O_3	bdl	0.03	bdl	bdl	0.05	bdl	0.13	bdl	bdl	na	na	na
MgO	bdl	bdl	bdl	bdl	0.02	0.01	bdl	bdl	bdl	bdl	bdl	0.09
CaO	55.21	54.96	55.36	55.15	53.65	54.73	54.86	55.16	55.32	51.33	49.94	53.10
SrO	bdl	0.19	0.04	bdl	bdl	bdl	0.02	0.02	0.02	0.14	0.14	0.11
PbO	bdl	bdl	bdl	bdl	bdl	bdl	bdl	bdl	bdl	0.12	0.04	0.17
MnO	0.04	0.07	0.06	0.03	1.32	1.22	0.62	0.75	0.64	1.62	1.16	0.50
FeO_{tot}	0.06	0.08	0.05	bdl	0.42	0.28	0.10	0.04	0.03	1.48	2.06	0.66
Na_2O	bdl	bdl	0.02	0.04	bdl	bdl	0.02	bdl	0.03	0.03	0.36	0.23
F	2.53	3.07	2.62	2.76	2.34	2.33	1.52	0.71	0.66	bdl	0.01	0.56
Cl	bdl	0.01	bdl	bdl	0.01	0.01	0.01	0.01	0.03	3.04	2.69	1.48
H_2O_{calc}	0.24	0.32	0.55	0.54	0.67	0.69	1.07	1.46	1.48	0.95	1.01	1.12
CO_{2calc}										0.53	0.8	1.68
O=F,Cl	-1.07	-1.29	-1.10	-1.16	-1.40	-0.98	-0.64	-0.31	-0.30	-0.69	-0.75	-0.74
Total	99.27	99.71	100.35	99.77	100.29	100.86	100.49	100.84	100.84	99.51	97.91	98.47
apfu***												
S	bdl	bdl	bdl	bdl	0.001	bdl	bdl	0.001	bdl	bdl	0.036	bdl
P	2.987	2.981	3.010	3.005	3.031	2.985	3.007	2.997	2.993	2.937	2.868	2.791
Si	0.015	0.018	0.007	0.004	0.003	0.010	0.008	0.020	0.016	bdl	bdl	0.014
C										0.063	0.096	0.195
Sum *T*	3.003	3.000	3.017	3.008	3.035	2.995	3.014	3.018	3.010	3.000	3.000	3.000
Al	0.002	0.003	0.003	0.002	0.002	0.001	0.004	0.004	0.002	bdl	bdl	bdl
Y	0.001	0.006	0.002	0.002	bdl	0.003	bdl	0.001	0.001	0.004	0.001	bdl
La	0.002	bdl	bdl	0.001	bdl	bdl	0.001	bdl	bdl	bdl	bdl	bdl
Ce	bdl	0.002	0.001	0.001	0.002	bdl	0.004	bdl	bdl	bdl	0.002	bdl
Pr	bdl	bdl	bdl	0.001	0.001	0.002	0.001	bdl	bdl			
Nd	0.001	0.002	0.001	bdl	0.002	0.001	bdl	bdl	bdl			
Sm	bdl	0.001	bdl	bdl	0.001	bdl	0.004	bdl	bdl			
Mg	bdl	bdl	bdl	bdl	0.003	0.001	bdl	bdl	bdl	bdl	bdl	0.011
Ca	4.983	4.964	4.963	4.969	4.831	4.890	4.917	4.916	4.927	4.754	4.674	4.858
Sr	bdl	0.009	0.002	bdl	bdl	bdl	0.001	0.001	0.001	0.007	0.007	0.005
Ba	bdl	bdl	bdl	0.007	bdl	bdl	bdl	0.004	0.008	bdl	bdl	bdl
Pb	bdl	bdl	bdl	bdl	bdl	bdl	bdl	bdl	bdl	0.003	0.001	0.004
Mn	0.003	0.005	0.004	0.002	0.094	0.086	0.044	0.053	0.045	0.119	0.086	0.036
Fe	0.004	0.006	0.004	bdl	0.030	0.020	0.007	0.003	0.002	0.107	0.150	0.047
Na	bdl	bdl	0.003	0.006	bdl	bdl	0.003	bdl	0.004	0.006	0.061	0.038
Sum M	4.996	4.994	4.983	4.992	4.965	5.005	4.986	4.982	4.990	5.00	5.00	5.0

This is the peer-reviewed, final accepted version for American Mineralogist, published by the Mineralogical Society of America.
The published version is subject to change. Cite as Authors (Year) Title. American Mineralogist, in press.
DOI: https://doi.org/10.2138/am-2023-9172. http://www.minsocam.org/

OH^-_{calc}	0.137	0.180	0.307	0.304	0.378	0.385	0.596	0.812	0.821	0.551	0.594	0.635
F	0.863	0.819	0.693	0.695	0.621	0.613	0.403	0.186	0.175	bdl	0.002	0.150
Cl	bdl	0.001	bdl	0.001	0.001	0.001	0.001	0.001	0.003	0.449	0.403	0.215
Sum X	1.000	1.000	1.000	1.000	1.000	1.000	1.000	1.000	1.000	1.000	1.000	1.00

* Notes: bdl – below detection limit, na – not analyzed. Mineral zone abbreviations are given in Table 1. Analysis numbers: 1–7, 10–12 from sample 61-89/240.5 m; 8, 9 from sample 61-89/241.5 m.

** Analyses 5 and 6 represent apatite in the aplite relics from the apatite zone (AP), and analysis 7 is from the triphylite zone (TR).

*** Content of cations was calculated on the basis of Σ(M+T) = 8 cations in A1-type apatite, and on the basis of ΣM = 5 cations in A3-type apatite.

This is the peer-reviewed, final accepted version for American Mineralogist, published by the Mineralogical Society of America.
The published version is subject to change. Cite as Authors (Year) Title. American Mineralogist, in press.
DOI: https://doi.org/10.2138/am-2023-9172. http://www.minsocam.org/

TABLE 5. Representative EMP and LA-ICP-MS analyses of A2-type apatite and triphylite from the AP, TR, and TRN zones.

Mineral	**Apatite**					**Triphylite**				
Zone	AP					TR			TRN	
Crystal parts / grain No.	core/1	rim/1	rim/1	core/2	rim/2	core/1	rim/1	core/2	core/3	rim/3
Analysis No.	1	2	3	4	5	1	2	3	4	5
EMP (wt%)										
SO_3	bdl	0.02	bdl	0.02	bdl	na	na	na	na	na
P_2O_5	42.06	42.06	42.30	42.21	42.34	46.45	46.67	46.32	46.23	46.67
CaO	54.08	54.43	54.75	54.16	54.94	0.05	0.02	0.02	bdl	0.02
FeO_{tot}	0.24	0.14	0.14	0.14	0.21	31.66	31.63	31.64	31.81	31.53
MnO	1.68	1.26	1.18	1.53	1.11	7.09	7.16	7.11	6.94	7.07
MgO	bdl	bdl	bdl	bdl	bdl	4.51	4.43	4.56	4.66	4.63
Li_2O*						9.76	9.78	9.76	9.77	9.79
F	2.05	2.11	2.20	2.10	2.03					
Cl	0.02	0.01	0.01	0.01	0.01					
H_2O_{calc}	0.81	0.78	0.75	0.79	0.83					
O=F	-1.23	-1.26	-1.32	-1.25	-1.22					
O=Cl	0.00	0.00	0.00	0.00	0.00					
Total	99.71	99.57	100.02	99.69	100.28	99.59	99.76	99.47	99.43	99.78
apfu**										
P	2.993	2.995	2.997	3.003	2.992	1.001	1.005	0.999	0.996	1.003
Ca	4.871	4.905	4.909	4.877	4.914	0.00	0.00	0.00	0.00	0.00
Mn	0.119	0.090	0.084	0.109	0.078	0.153	0.154	0.154	0.150	0.152
Mg	bdl	bdl	bdl	bdl	bdl	0.171	0.168	0.173	0.177	0.175
Fe	0.017	0.010	0.010	0.010	0.015	0.674	0.673	0.674	0.677	0.669
F^-	0.545	0.561	0.583	0.557	0.536					
Cl^-	0.002	0.001	0.001	0.001	0.001					
OH^-_{calc}	0.453	0.438	0.416	0.442	0.462					
Fe#						0.815	0.814	0.815	0.819	0.815
Fe##						0.675	0.676	0.674	0.675	0.671
LA-ICP-MS (ppm)										
Li (ppm)	7	28	43	8	36	49184	46864	46543	48011	51862
Si	<1817	<1553	<1764	<1767	<1782	<1763	<1947	<1692	<1539	<1831
Al	<10	<14	<9	<11	48	<13	<12	<14	<12	49
Mg	60.3	241.3	24.1	6.0	79.4					
Na	108.6	98.2	87.3	135.9	140.5	4.0	24.9	10.7	5.6	16.3
Sc	6.6	2.4	4.3	10.5	5.2	29.4	31.2	30.2	17.9	9.7
Co	<0.57	<0.7	<0.8	<1.04	<0.7	9.7	7.7	7.9	8.4	8.5
Zn	<7.7	17	<6.9	<8.3	<8.9	863.9	1005.9	884.8	892.2	949.6
Ga	<1.4	2.5	1.1	1.6	<1.4	<1.5	1.8	<1.8	2.5	<2.2
Sr	100.6	95.5	90.1	98.1	86.0	<0.4	35.7	5.7	<0.2	8.1

This is the peer-reviewed, final accepted version for American Mineralogist, published by the Mineralogical Society of America.
The published version is subject to change. Cite as Authors (Year) Title. American Mineralogist, in press.
DOI: https://doi.org/10.2138/am-2023-9172. http://www.minsocam.org/

Y	142.8	133.4	129.0	178.8	176.0	<0.4	<0.2	<0.1	<0.3	<0.1
Zr	1.0	1.4	<0.4	0.8	0.3	<0.3	<0.6	<0.5	0.4	<0.6
Sn	12.6	11.9	<0.4	1.3	<0.9	1.0	<0.6	<0.7	<0.8	<0.9
La	32.7	29.6	29.3	40.6	39.3	<0.1	<0.2	<0.2	<0.1	<0.1
Ce	64.9	63.8	64.0	88.7	85.5	<0.1	<0.2	<0.1	<0.2	<0.1
Pr	8.0	7.8	6.9	9.6	9.5	<0.1	<0.1	<0.1	<0.1	<0.1
Nd	35.3	32.7	31.4	41.3	38.4	<0.6	<0.5	<0.7	<1.0	<1.3
Sm	11.6	14.5	9.4	25.3	18.2	<1.6	<2.2	<1.5	<1.5	<1.7
Eu	4.4	5.5	5.4	3.2	3.9	<0.3	<0.2	0.3	<0.3	<0.3
Gd	21.5	17.2	16.0	27.7	27.1	<1.1	<0.8	<0.8	<0.8	<0.9
Tb	4.2	4.0	3.8	7.4	7.8	<0.1	<0.1	<0.2	<0.1	<0.2
Dy	28.6	22.8	22.3	33.2	35.4	<0.6	0.5	<0.7	<0.5	<0.5
Ho	4.5	4.4	3.6	4.8	4.3	<0.1	<0.1	<0.1	<0.1	<0.2
Er	12.2	9.7	10.9	10.5	9.5	<0.6	<0.4	<0.4	<0.5	<0.4
Tm	1.4	1.7	1.2	1.6	1.7	<0.1	<0.1	<0.2	<0.1	<0.1
Yb	9.7	9.3	9.7	10.7	9.8	<1.4	<0.8	0.7	<1.1	<0.9
Lu	1.2	1.4	1.5	1.6	1.4	<0.1	<0.2	<0.1	<0.2	<0.2
Pb	17.0	28.7	5.4	15.8	9.0	<0.3	<0.3	0.4	<0.3	<0.4
Bi	1.8	1.5	0.5	1.3	0.6	<0.4	<0.2	0.2	<0.2	<0.6
Th	103.4	74.8	33.9	108.4	49.1	<0.3	<0.3	<0.2	<0.2	<0.1
U	312.5	310.0	211.6	418.1	362.4	<0.1	0.3	<0.1	<0.1	<0.1
LREE	160	156	147	212	195					
(HREE+Y)	230	206	199	281	273					
LREE/ (HREE+Y)	0.41	0.43	0.43	0.43	0.42					

* Notes: na – not analyzed, bdl – below detection limit. Mineral zone abbreviations are given in Table 1. All analyses were carried out on sample 61-89/240.5 m. Li and Li_2O contents listed for EMP analyses were computed on the basis of an ideal sum of Li = 1.00 apfu.

** Content of ions was calculated on the basis of 13 O and 8 cations in apatite, and on the basis of 4 O and 3 cations in triphylite.

This is the peer-reviewed, final accepted version for American Mineralogist, published by the Mineralogical Society of America.
The published version is subject to change. Cite as Authors (Year) Title. American Mineralogist, in press.
DOI: https://doi.org/10.2138/am-2023-9172. http://www.minsocam.org/

TABLE 6. Representative compositions (wt%) of triphylite, as determined by EMP.*

Zones	**PGM**			**AP**					**Triphylite rods**			
Analysis No.	1	2	3	4	5	6	7	8	9	10	11	12
P_2O_5	45.48	45.63	45.71	46.61	46.16	45.78	45.89	46.59	45.35	45.95	45.91	46.19
SiO2	0.20	0.18	0.13	bdl	0.02	0.26	0.22	0.07	bdl	bdl	bdl	bdl
Al_2O_3	0.03	0.04	0.02	bdl	bdl	0.01	0.02	bdl	bdl	bdl	bdl	bdl
FeO_{tot}	34.26	35.03	34.86	28.64	28.64	28.68	29.19	28.91	26.86	28.19	28.61	27.43
MnO	6.80	6.88	6.94	11.32	11.23	11.51	11.04	10.80	12.01	10.60	10.13	11.80
MgO	2.08	1.88	1.88	2.90	2.94	2.84	3.06	3.13	3.06	2.95	3.17	2.48
CaO	bdl	0.04	0.03	0.35	0.42	0.31	0.34	0.73	0.68	0.83	0.72	0.81
SrO	0.04	0.04	bdl	0.17	na	na	na	na	bdl	0.04	bdl	0.03
Na_2O	0.04	0.04	0.02	bdl	bdl	bdl	bdl	0.01	0.05	0.07	bdl	bdl
ZnO	0.43	0.31	0.30	0.24	0.06	0.08	0.03	0.02	0.10	0.19	0.30	0.12
Li_2O	9.53	9.59	9.57	9.69	9.63	9.62	9.67	9.74	9.51	9.58	9.58	9.54
Total	98.90	99.67	99.46	99.92	99.10	99.12	99.46	100.01	97.60	98.41	98.42	98.40
Content of ions on the basis of 4 O and 3 cations, apfu												
P	1.004	1.001	1.005	1.012	1.009	1.001	0.999	1.007	1.004	1.010	1.008	1.020
Si	0.005	0.005	0.003	bdl	0.001	0.007	0.006	0.002	bdl	bdl	bdl	bdl
Σ T	1.010	1.006	1.009	1.012	1.010	1.008	1.004	1.009	1.004	1.010	1.008	1.020
Al	0.001	0.001	bdl	bdl	bdl	bdl	0.001	bdl	bdl	bdl	bdl	bdl
Ca	bdl	0.001	0.001	0.010	0.012	0.008	0.009	0.020	0.019	0.023	0.020	0.023
Sr	0.001	0.001	bdl	0.003	na	na	na	Na	bdl	0.001	bdl	bdl
Mn	0.150	0.151	0.153	0.246	0.246	0.252	0.240	0.234	0.266	0.233	0.222	0.261
Mg	0.081	0.073	0.073	0.111	0.113	0.110	0.117	0.119	0.119	0.114	0.122	0.096
Fe	0.747	0.759	0.757	0.614	0.619	0.620	0.628	0.617	0.587	0.612	0.621	0.598
Zn	0.008	0.006	0.006	0.005	0.001	0.002	bdl	bdl	0.002	0.004	0.006	0.002
Na	0.002	0.002	0.001	bdl	bdl	bdl	bdl	0.001	0.002	0.004	bdl	bdl
Li	1.000	1.000	1.000	bdl	1.000	1.000	1.000	1.000	1.000	1.000	1.000	1.000
Σ M	1.990	1.994	1.991	1.988	1.990	1.992	1.996	1.991	1.996	1.990	1.992	1.980
Fe/ (Fe+Mn)	0.83	0.83	0.83	0.72	0.72	0.71	0.72	0.73	0.69	0.72	0.74	0.70
Fe/ (Fe+Mn+Mg)	0.76	0.77	0.77	0.63	0.63	0.63	0.64	0.64	0.60	0.64	0.64	0.63

*Notes: na – not analyzed, bdl – below detection limit; mineral zone abbreviations are given in Table 1. Analysis numbers:1–3 for triphylite crystals from sample 61-89/241.5 m; 4–8 for interstitial triphylite from sample 61-89/240.5 m; 9–12 for triphylite rods in A2-type apatite from sample 61-89/240.5 m. Li and Li_2O contents were computed on the basis of an ideal sum of Li = 1.00 apfu.

Figure 1

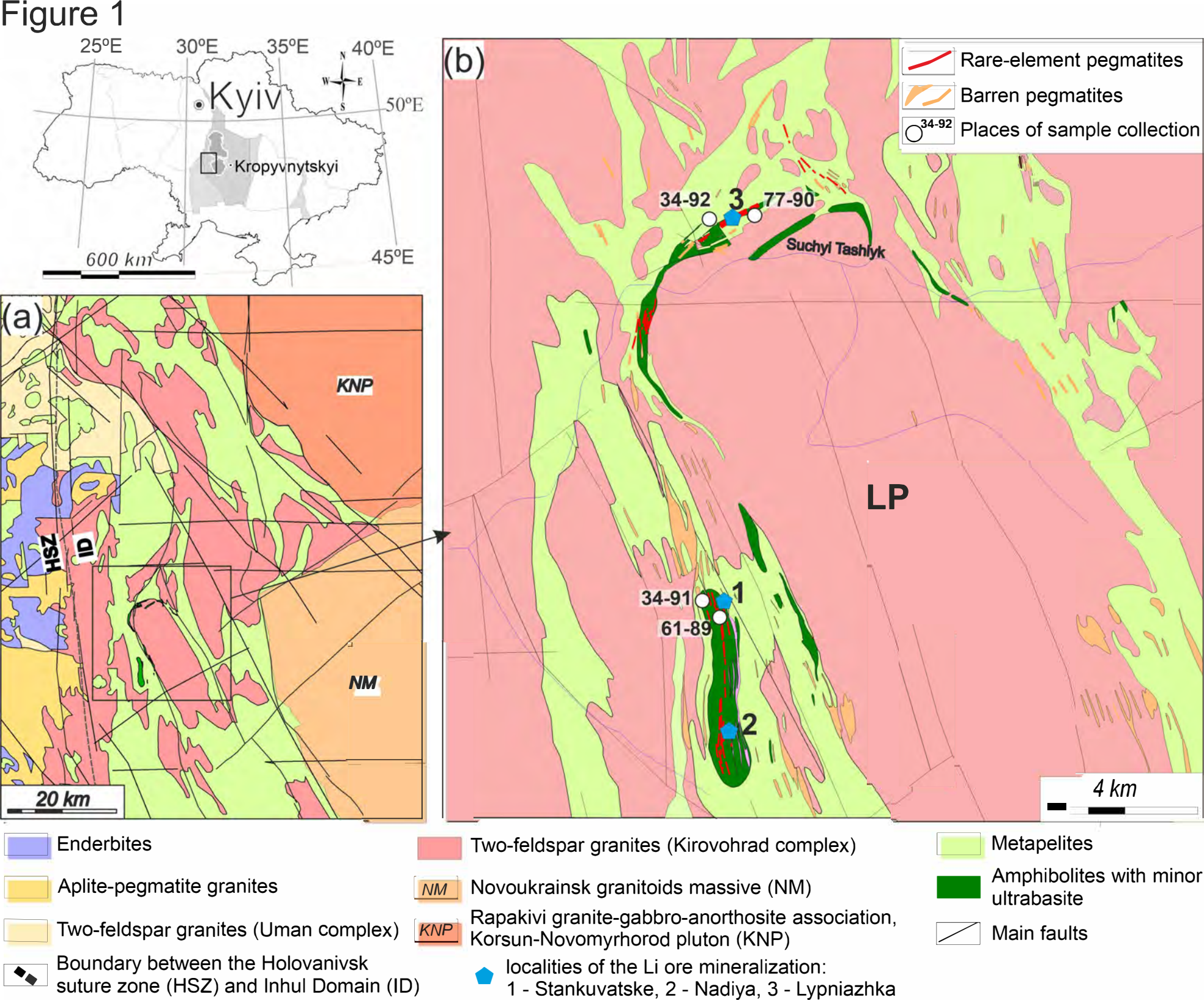
25°E
30°E
35°E
40°E
45°E
50°E
Kyiv
Kropyvnytskyi
600 km
(a)
KNP
NM
HSZ
ID
20 km
(b)
Rare-element pegmatites
Barren pegmatites
34-92
Places of sample collection
34-92
3
77-90
Suchyi Tashlyk
LP
34-91
1
61-89
2
4 km
Enderbites
Aplite-pegmatite granites
Two-feldspar granites (Uman complex)
Boundary between the Holovanivsk suture zone (HSZ) and Inhul Domain (ID)
Two-feldspar granites (Kirovohrad complex)
NM
Novoukrainsk granitoids massive (NM)
KNP
Rapakivi granite-gabbro-anorthosite association, Korsun-Novomyrhorod pluton (KNP)
localities of the Li ore mineralization:
1 - Stankuvatske, 2 - Nadiya, 3 - Lypniazhka
Metapelites
Amphibolites with minor ultrabasite
Main faults

Figure 2

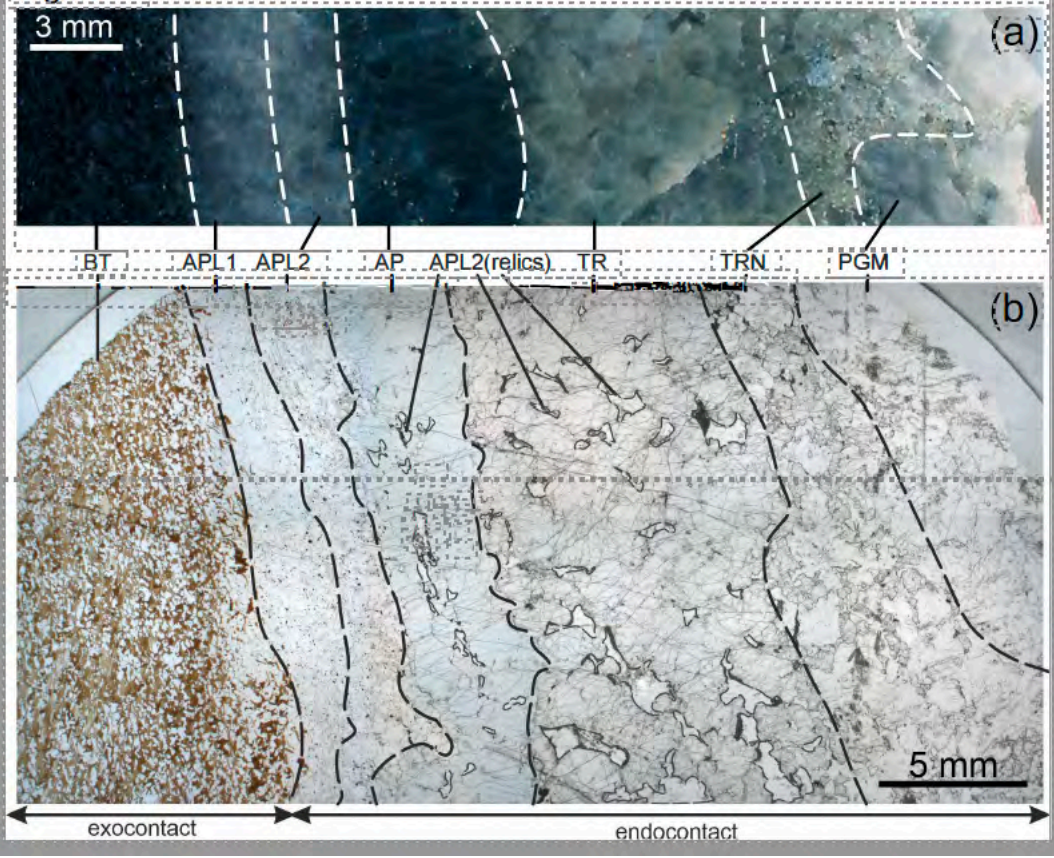
3 mm
(a)
BT
APL1
APL2
AP
APL2(relics)
TR
TRN
PGM
(b)
5 mm
exocontact
endocontact

Figure 3

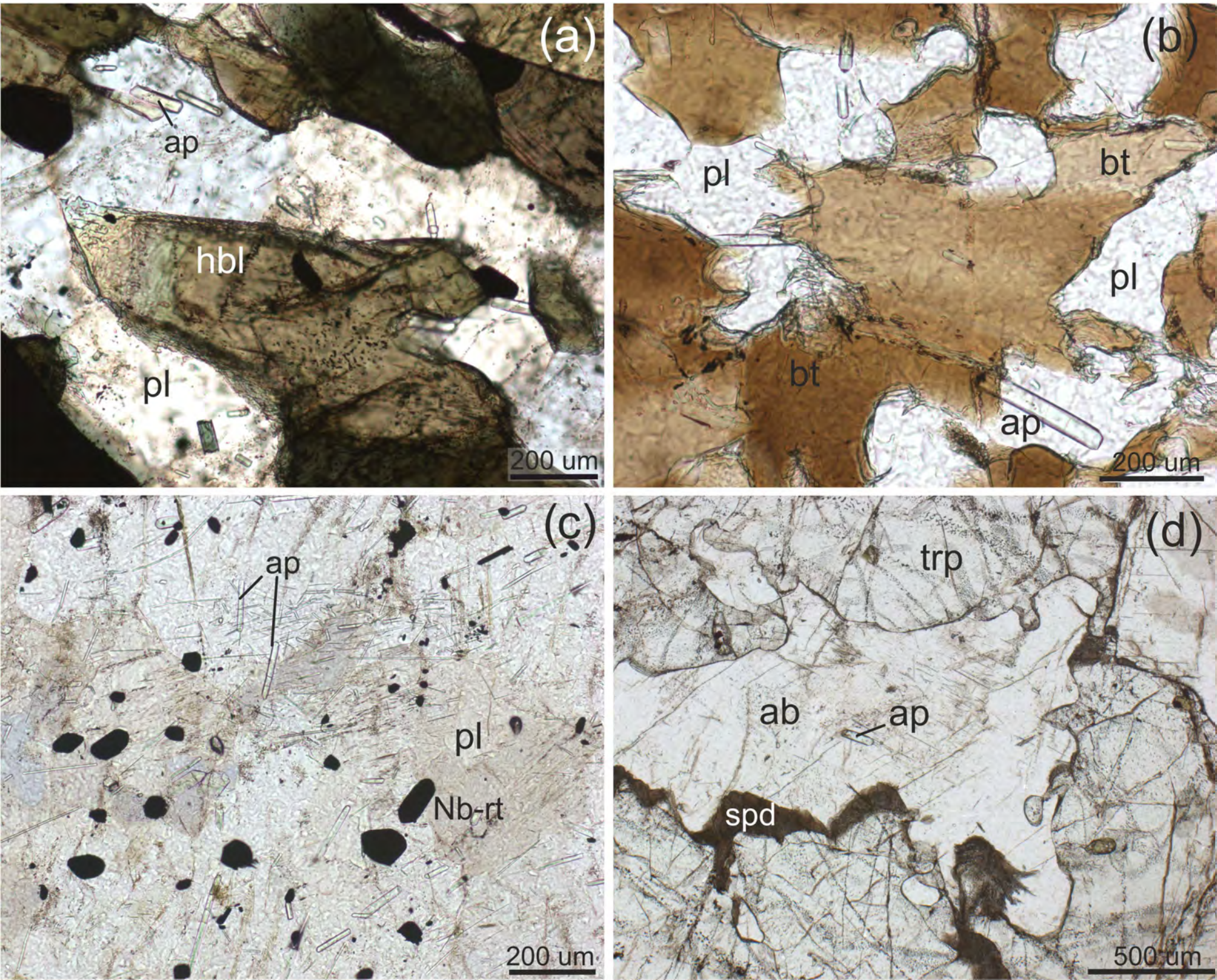
(a)
ap
hbl
pl
200 um
(b)
pl
bt
pl
bt
ap
200 um
(c)
ap
pl
Nb-rt
200 um
(d)
trp
ab
ap
spd
500 um

Figure 4

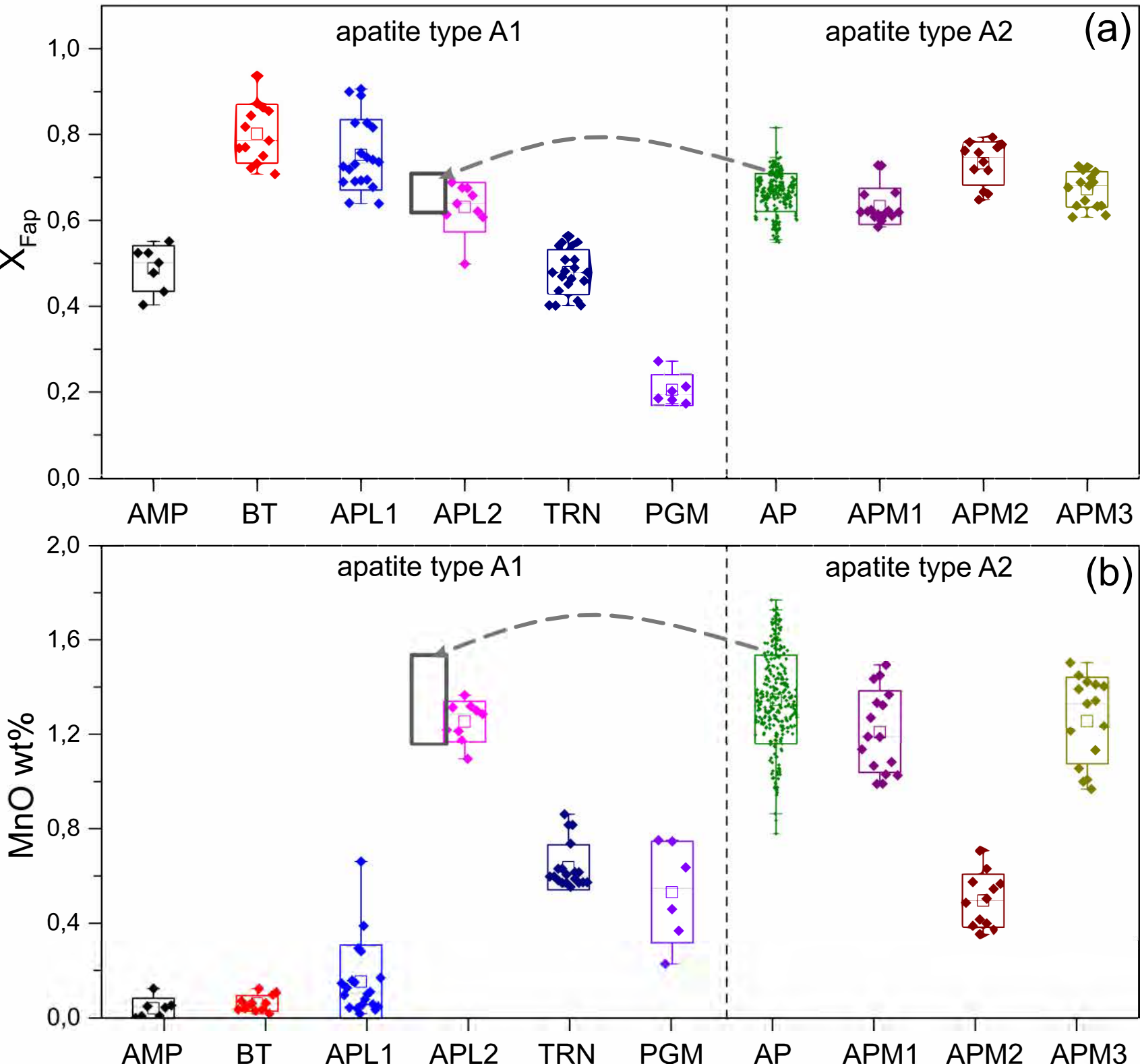
apatite type A1
apatite type A2
(a)
X_{Fap}
1,0
0,8
0,6
0,4
0,2
0,0
AMP
BT
APL1
APL2
TRN
PGM
AP
APM1
APM2
APM3
apatite type A1
apatite type A2
(b)
MnO wt%
2,0
1,6
1,2
0,8
0,4
0,0
AMP
BT
APL1
APL2
TRN
PGM
AP
APM1
APM2
APM3

Figure 5

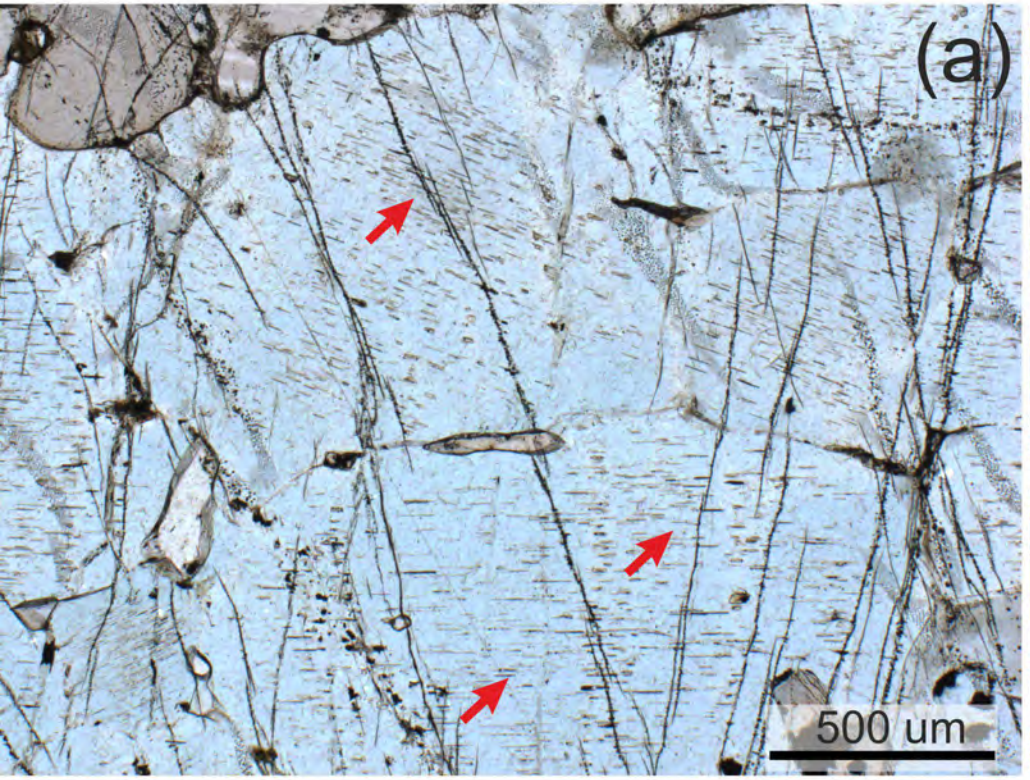

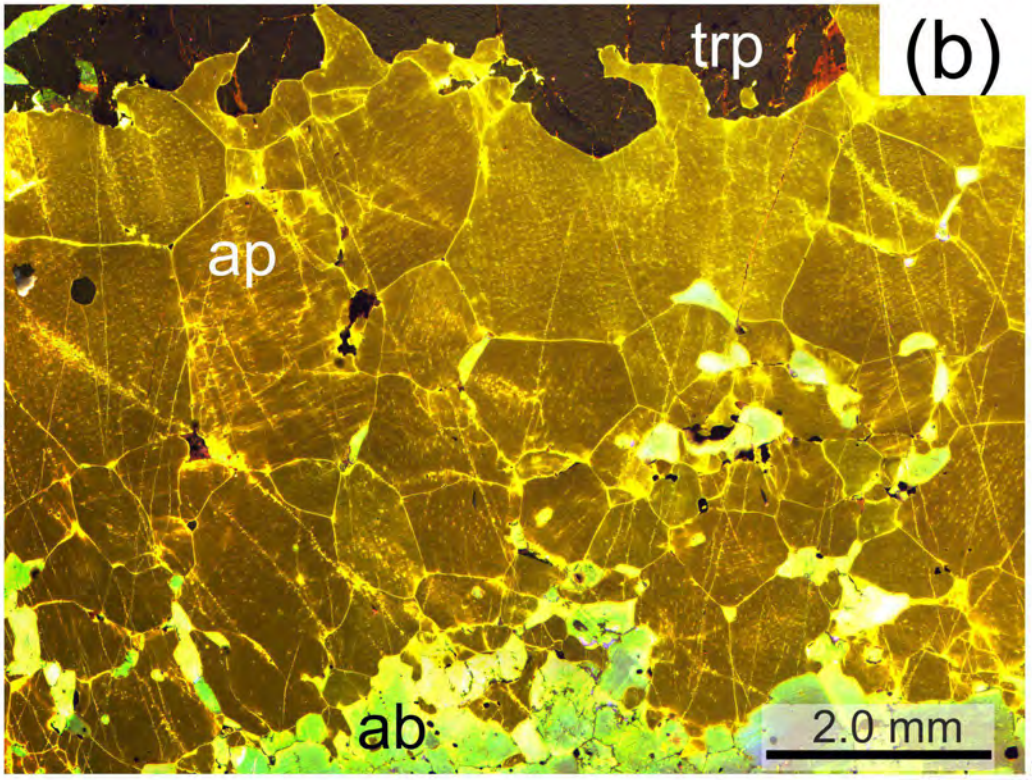

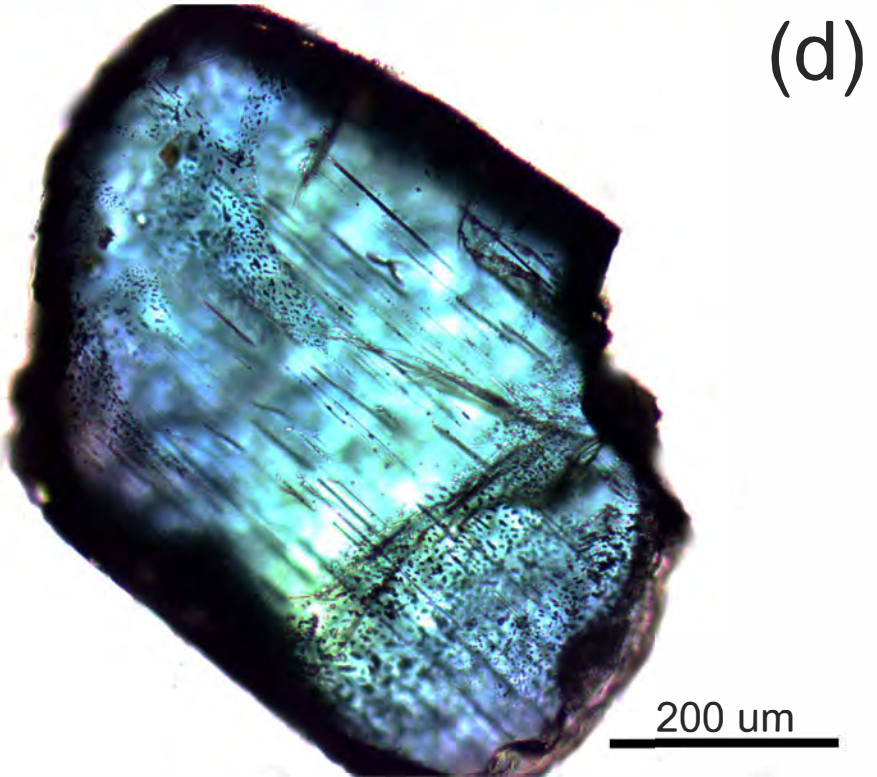

Figure 6

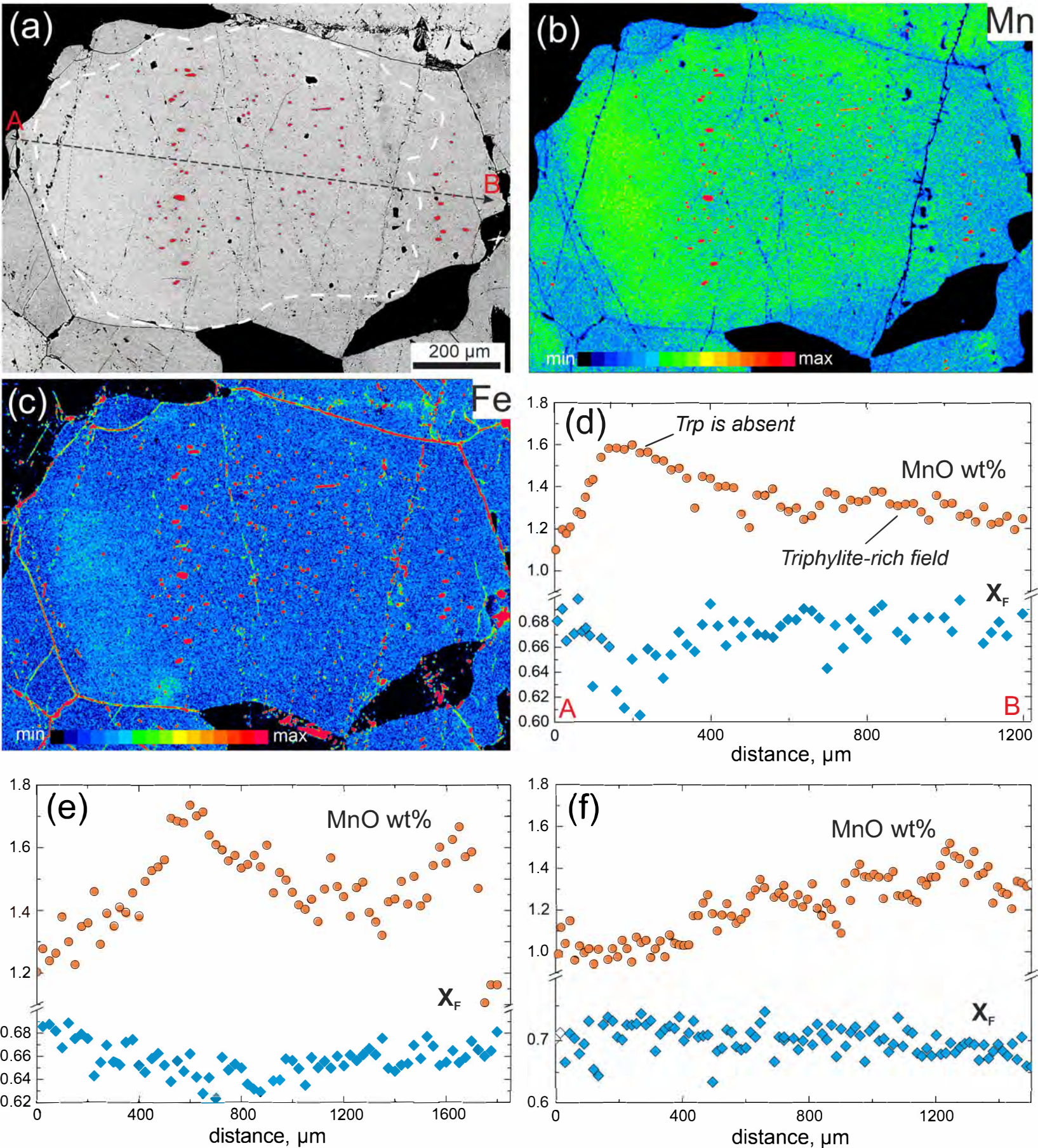
(a)
A
B
200 μm
(b)
Mn
min
max
(c)
Fe
min
max
(d)
Trp is absent
MnO wt%
Triphylite-rich field
X_F
A
B
1.8
1.6
1.4
1.2
1.0
0.68
0.66
0.64
0.62
0.60
0
400
800
1200
distance, μm
(e)
MnO wt%
X_F
1.8
1.6
1.4
1.2
0.68
0.66
0.64
0.62
0
400
800
1200
1600
distance, μm
(f)
MnO wt%
X_F
1.8
1.6
1.4
1.2
1.0
0.7
0.6
0
400
800
1200
distance, μm

Figure 7

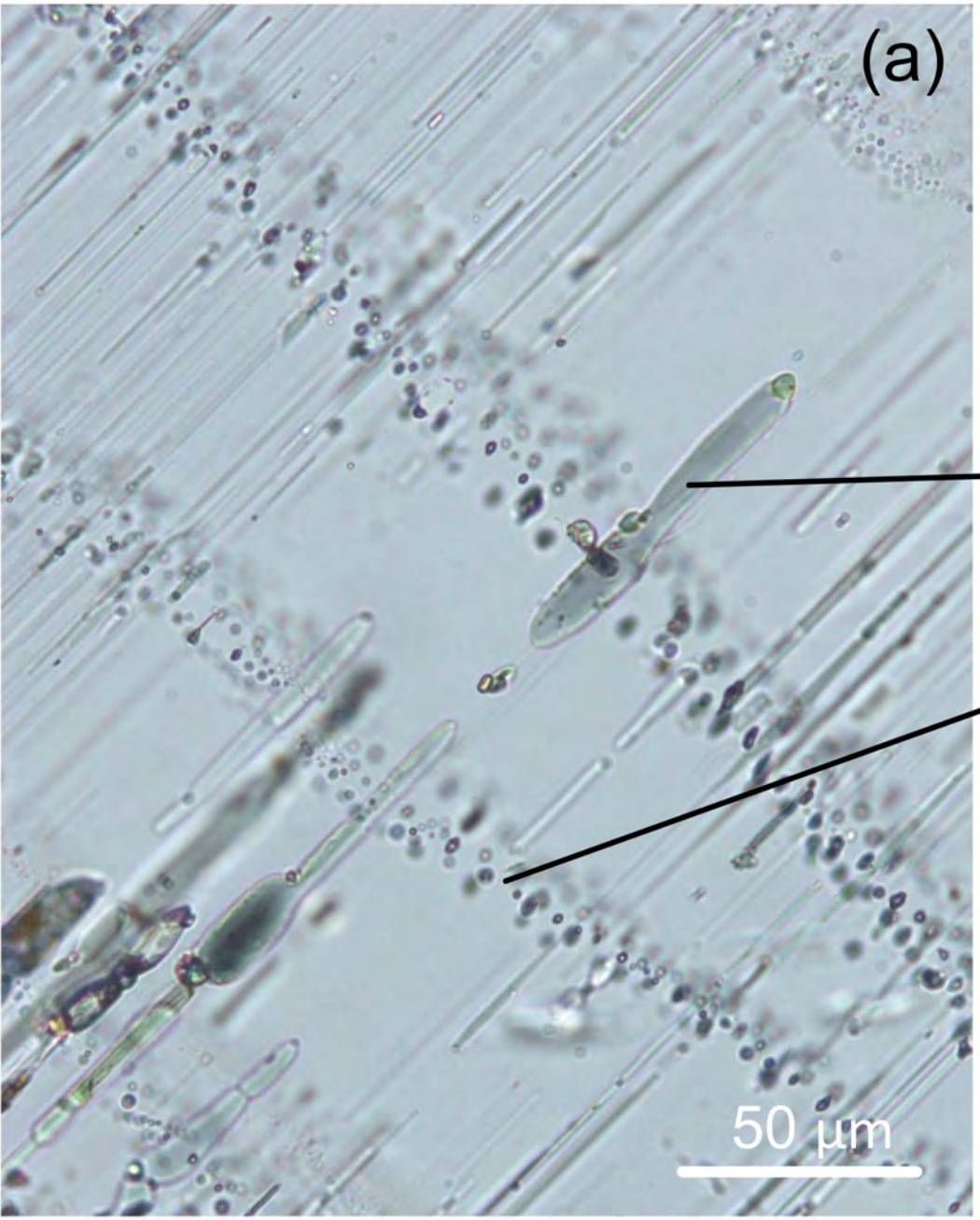
(a)
50 µm

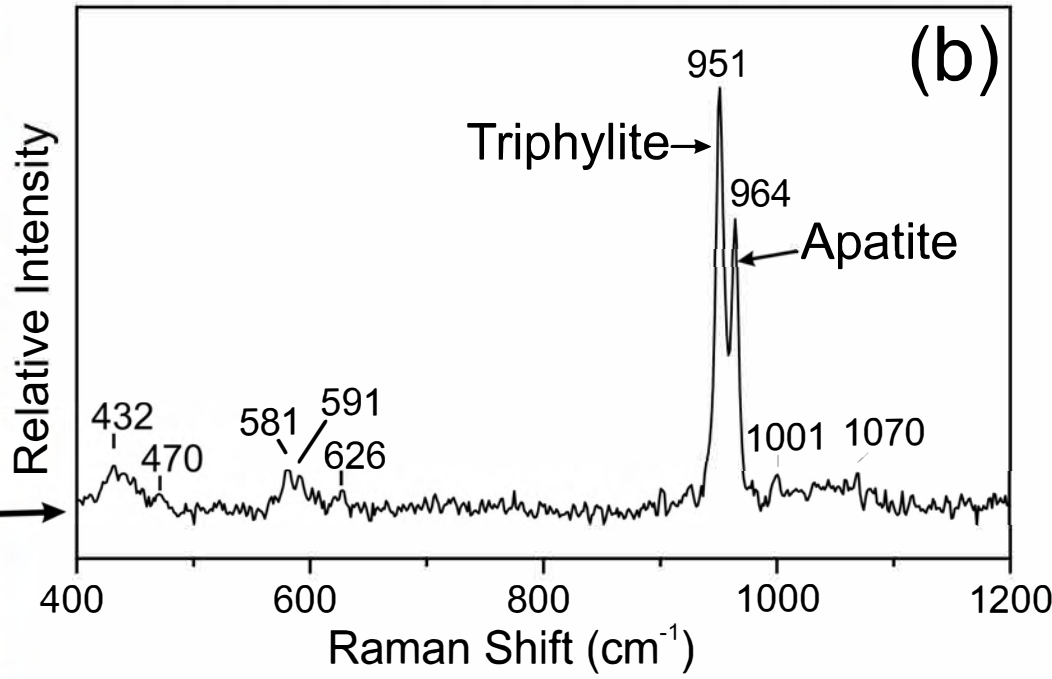
(b)
951
Triphylite
964
Apatite
432
470
581
591
626
1001
1070
Relative Intensity
400
600
800
1000
1200
Raman Shift (cm-1)

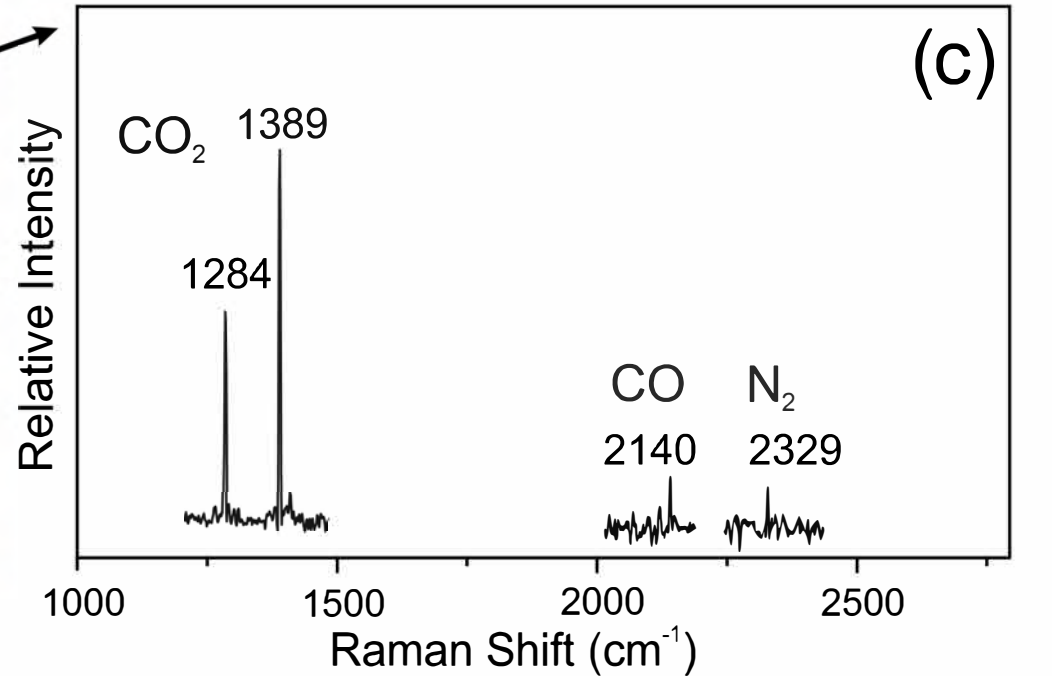
(c)
CO2
1389
1284
CO
2140
N2
2329
Relative Intensity
1000
1500
2000
2500
Raman Shift (cm-1)

Figure 8

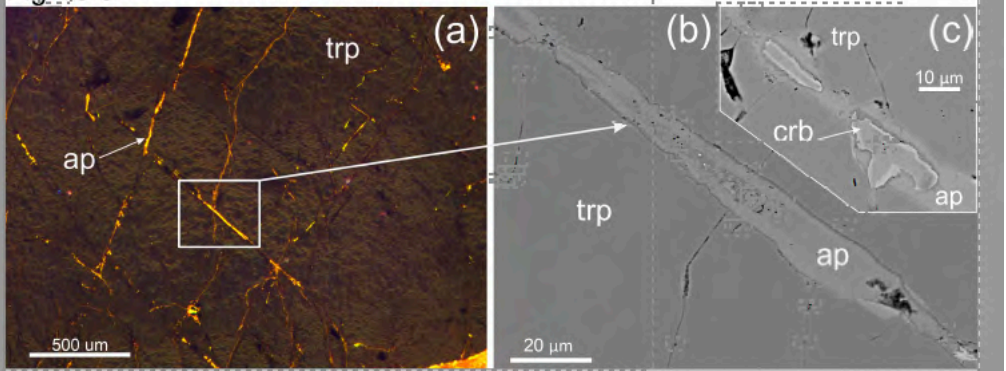

Figure 9

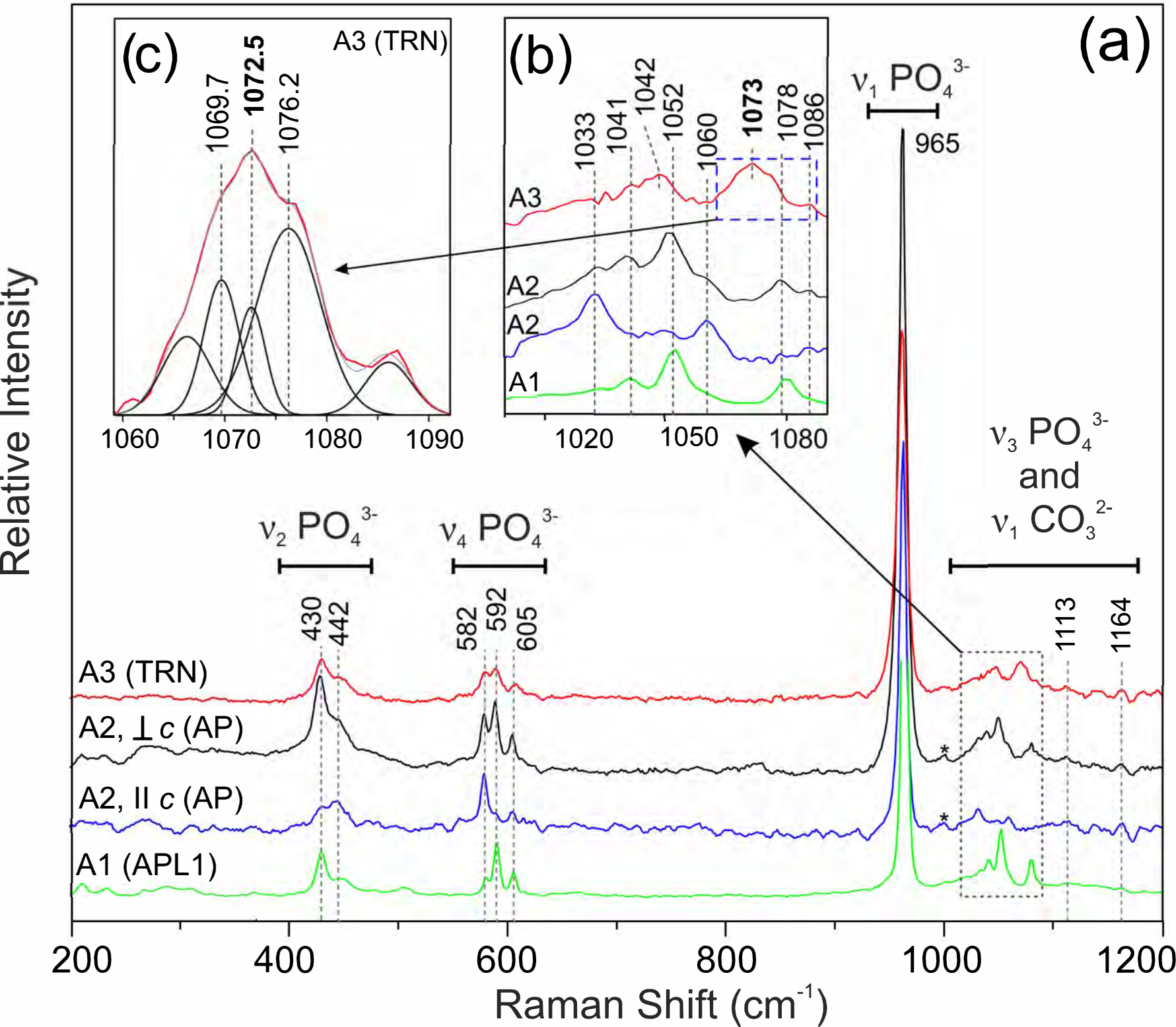
(a)
(b)
(c)
A3 (TRN)
A2, ⊥ c (AP)
A2, II c (AP)
A1 (APL1)
A3
A2
A2
A1
ν1 PO4 3-
965
ν3 PO4 3-
and
ν1 CO3 2-
ν2 PO4 3-
ν4 PO4 3-
430
442
582
592
605
1113
1164
1033
1041
1042
1052
1060
1073
1078
1086
1069.7
1072.5
1076.2
1060
1070
1080
1090
1020
1050
1080
200
400
600
800
1000
1200
Relative Intensity
Raman Shift (cm-1)

Figure 10

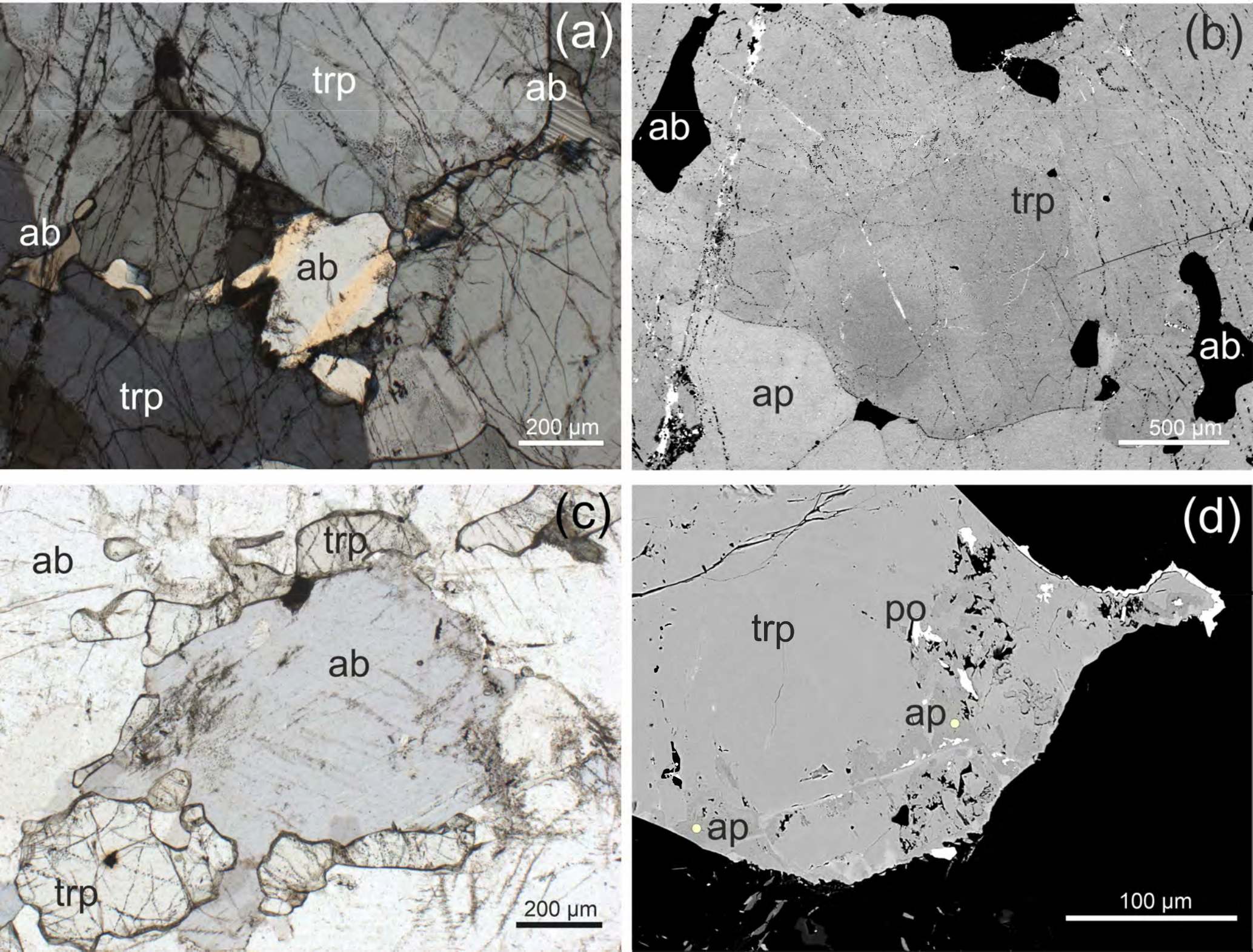
(a)
trp
ab
ab
ab
trp
200 µm
(b)
ab
trp
ap
ab
500 µm
(c)
ab
trp
ab
trp
200 µm
(d)
trp
po
ap
ap
100 µm

Figure 11

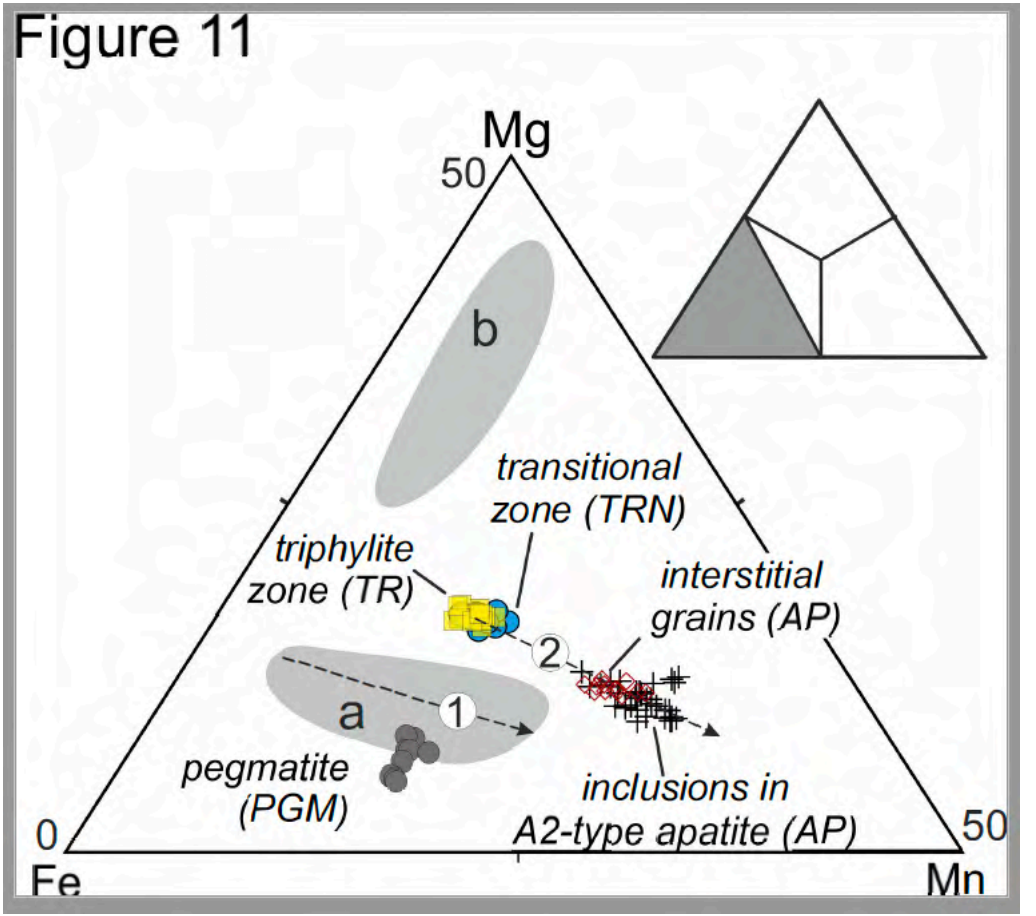
Mg
50
b
transitional
zone (TRN)
triphylite
zone (TR)
interstitial
grains (AP)
2
a
1
pegmatite
(PGM)
inclusions in
A2-type apatite (AP)
0
50
Fe
Mn

Figure 12

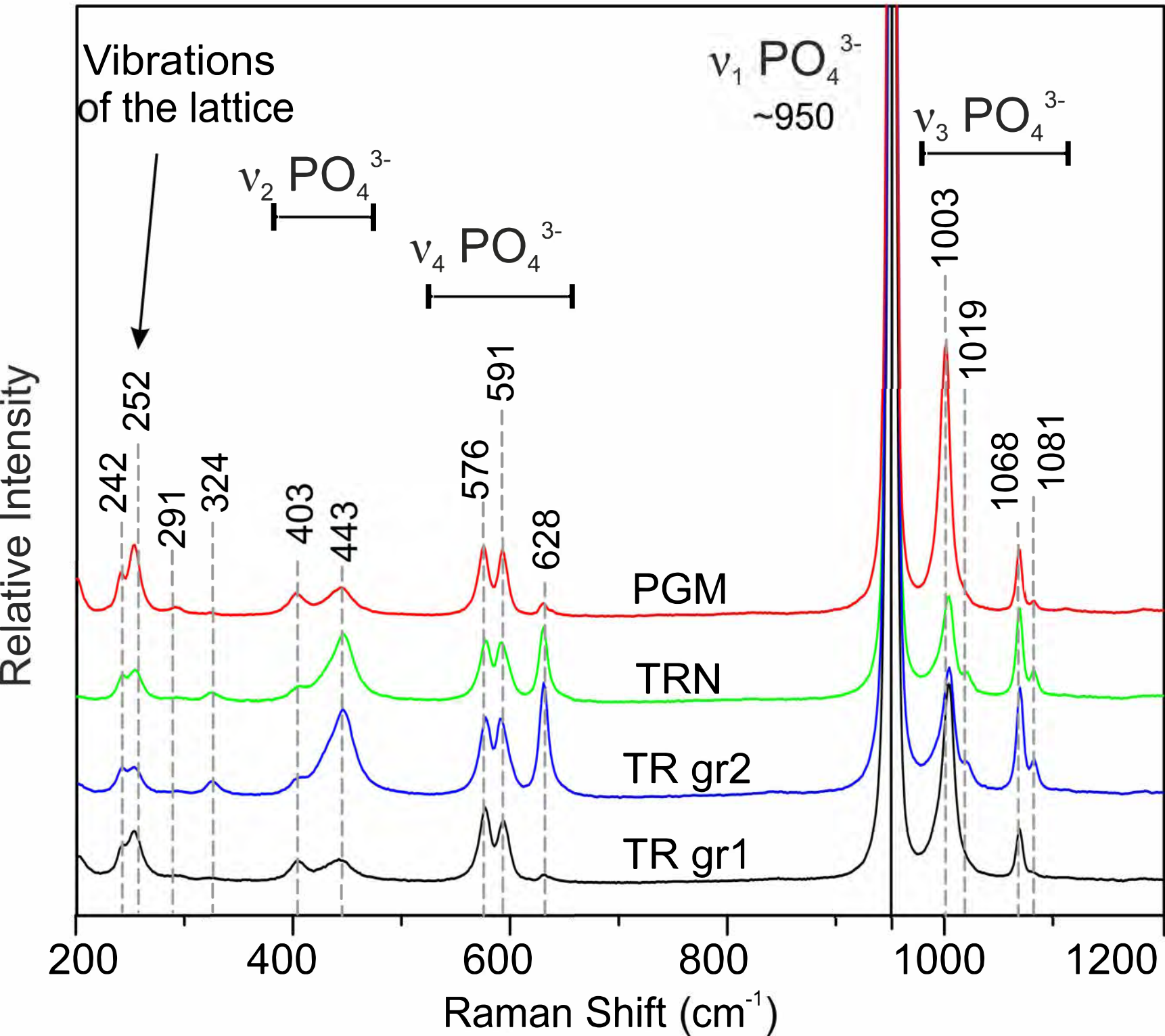
Vibrations
of the lattice
ν_1 PO_4^{3-}
~950
ν_3 PO_4^{3-}
ν_2 PO_4^{3-}
ν_4 PO_4^{3-}
1003
1019
1068
1081
591
252
242
291
324
403
443
576
628
PGM
TRN
TR gr2
TR gr1
Relative Intensity
200
400
600
800
1000
1200
Raman Shift (cm^{-1})

Figure 13

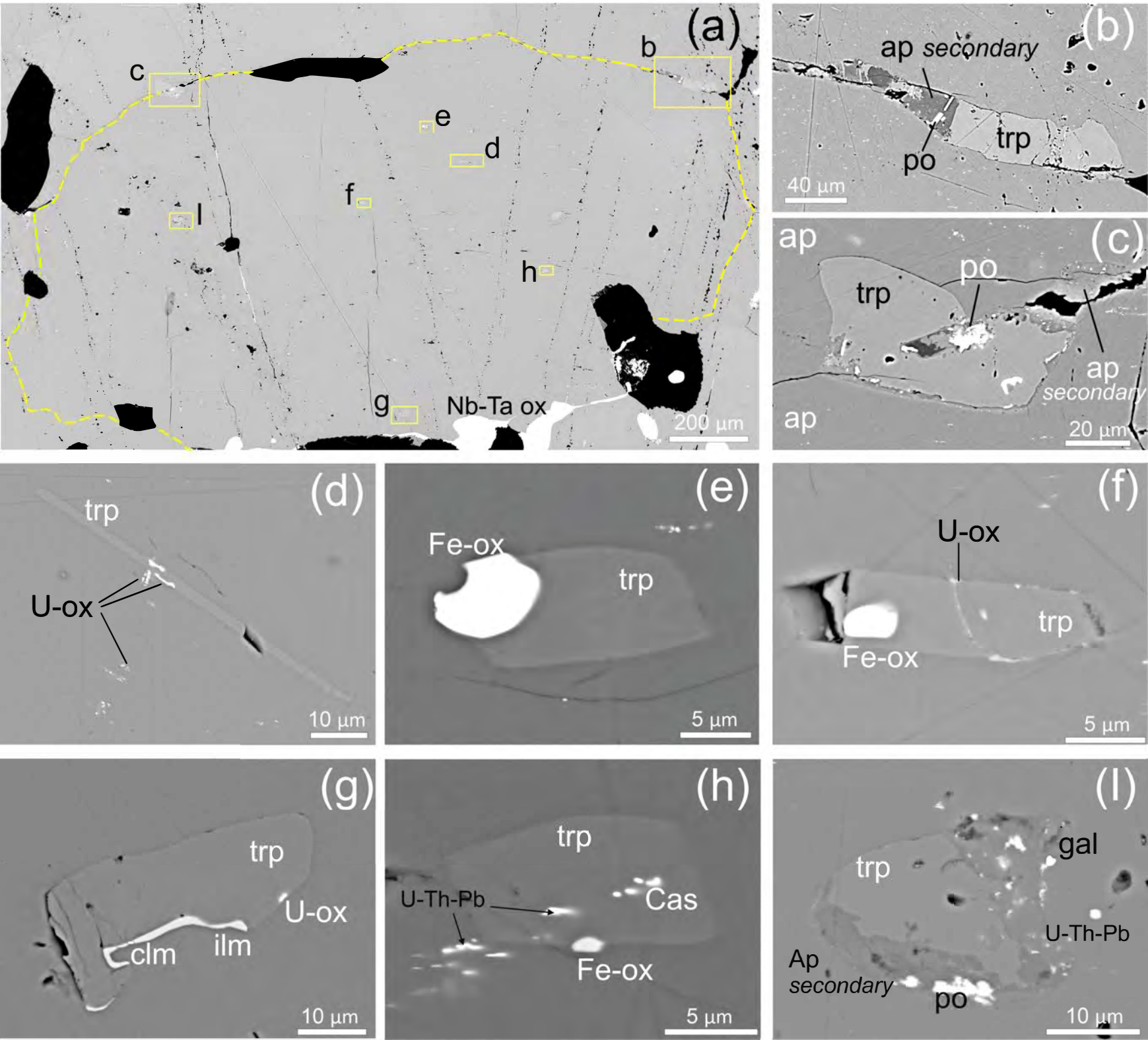
(a)
b
c
e
d
f
l
h
g
Nb-Ta ox
200 µm
(b)
ap secondary
trp
po
40 µm
ap
(c)
po
trp
ap
secondary
ap
20 µm
(d)
trp
U-ox
10 µm
(e)
Fe-ox
trp
5 µm
(f)
U-ox
trp
Fe-ox
5 µm
(g)
trp
U-ox
clm
ilm
10 µm
(h)
trp
U-Th-Pb
Cas
Fe-ox
5 µm
(l)
gal
trp
U-Th-Pb
Ap
secondary
po
10 µm

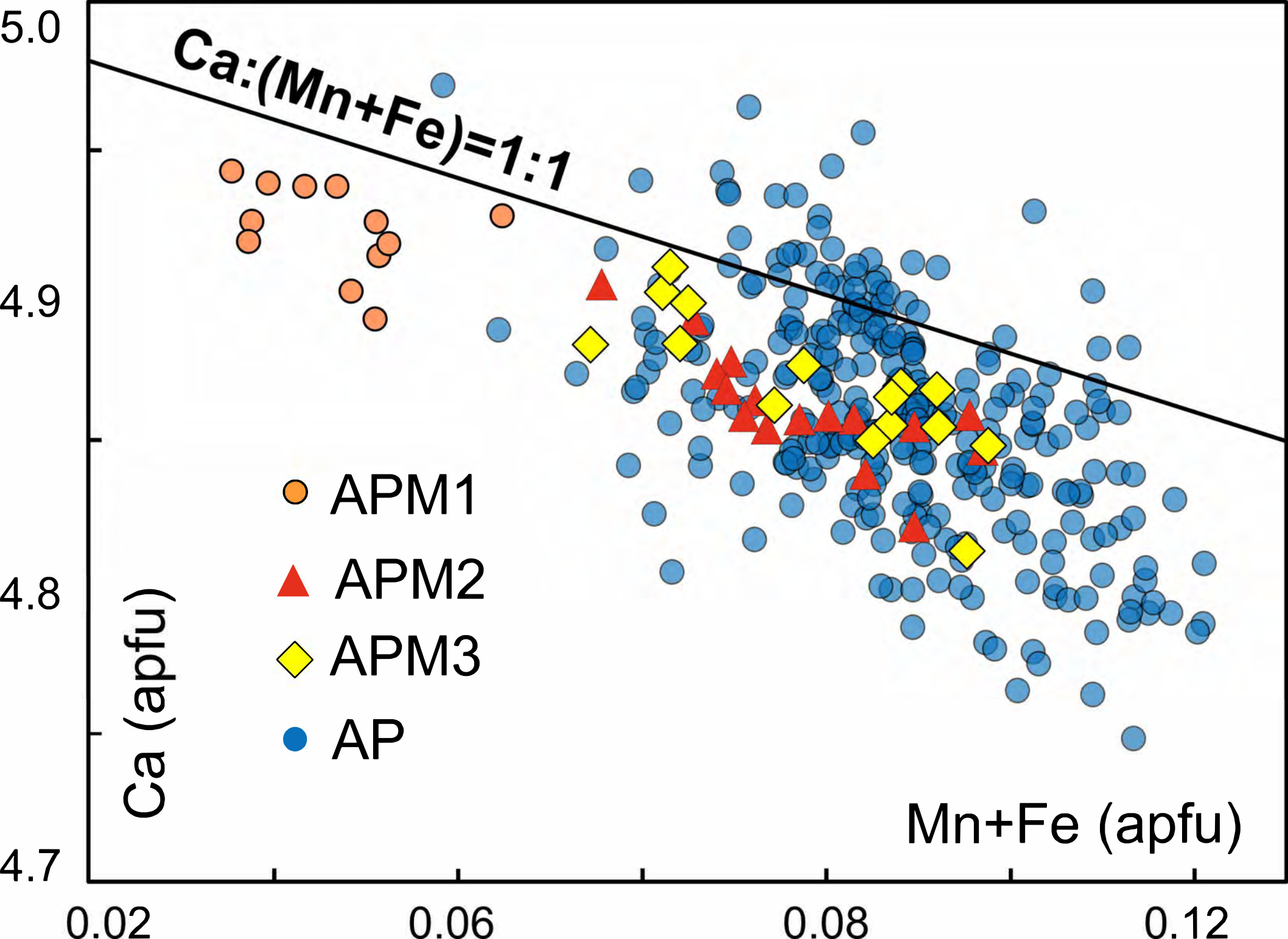
Ca:(Mn+Fe)=1:1
APM1
APM2
APM3
AP
Ca (apfu)
Mn+Fe (apfu)
5.0
4.9
4.8
4.7
0.02
0.06
0.08
0.12